AN EXAMINATION OF THE RESISTANCE SPOT WELDING PROCESS OF THE ULTRA-HIGH-STRENGTH STEEL WITH EXPERIMENTAL AND NUMERICAL METHODS

ULTRA YÜKSEK DAYANIMLI ÇELİKLERDE NOKTA DİRENÇ KAYNAĞININ NÜMERİK VE DENEYSEL METOT İLE İNCELENMESİ

GİZEM AY

ASSIST. PROF. DR. MEHMET OKAN GÖRTAN

Supervisor

Submitted to

Graduate School of Science and Engineering of Hacettepe University

as a Partial Fulfillment to the Requirements

for the Award of Degree of Master of Science

in Mechanical Engineering.

2022

ABSTRACT

AN EXAMINATION OF THE RESISTANCE SPOT WELDING PROCESS OF THE ULTRA-HIGH-STRENGTH STEEL WITH EXPERIMENTAL AND NUMERICAL METHODS

Gizem AY

Master's Degree, Department of Mechanical Engineering

Supervisor: Assist. Prof. Dr. Mehmet Okan Görtan

May 2022, 61 pages

Since ultra-high-strength steels are being preferred in the automotive industry, the weldability of these steels has been gaining importance. When the scientific literature on the resistance spot weldability of UHSS is investigated, it is seen that additional studies are needed to fully understand this process. So, the motivation of this study is to get more information through numerical, and experimental methods about the resistance spot welding process of UHSS. In this study, the finite element model of the RSW process was generated as an axisymmetric and fully electrical-thermal-mechanical coupled via MSC. Marc software. MS1500 ultra high strength steel is selected as workpieces, and this process included the joining of the workpieces with the same sheet thicknesses (1.2 mm) and the same material in this study. This study provided a prediction of the quality, shape of the weld nugget, and the predicted temperature distribution via finite element

simulations with the variations of process parameter which is current values. Firstly, two main simulation were generated with 8 kA ideal sinusoidal alternative current, and alternative current with phase shift to convergence of the finite element models for the real RSW process. As a result, the heat generation amount for the ideal sinusoidal alternative current is higher than the phase shifted current one during welding time. Comparing the simulation results with physical experiments, the alternative current with phase shift was preferable to constructing the FE model of the RSW process. When comparing the experimental results and the results of generated simulation with 8 kA phase shifted current, there is a relatively minor 2% error in the diameter length and 40% error in nugget thickness at the last welding cycle. The nugget shape in the experimental result was an ellipse, however, the nugget shape in the simulation result was a flat ellipse. After that, all simulation model were generated with the phase shifted current values of 7; 7.5; 8.5; 9; 9.5 and 10 kA for different simulation models. Based on the simulation results, the nugget diameter increases as the phase shifted current value increases. However, as the current value increases, temperature values between workpiece/workpiece and workpiece/electrode have increased because the energy input in the welding cycles increases. As a consequence, material melting between workpiece/electrode was visible in the generated simulation with 8.5; 9; 9.5 and 10 kA phase shifted current.

ÖZET

ULTRA YÜKSEK DAYANIMLI ÇELİKLERDE NOKTA DİRENÇ KAYNAĞININ NÜMERİK VE DENEYSEL METOT İLE İNCELENMESİ

Gizem AY

Yüksek lisans, Makine Mühendisliği Bölümü

Tez Danışmanı: Assist. Prof. Dr. Mehmet Okan Görtan

Mayıs 2022, 61 sayfa

Otomotiv endüstrisinde ultra yüksek dayanımlı çelikler tercih edildiğinden beri, bu çeliklerin kaynaklanabilirliği önem kazanmaktadır. Ultra yüksek dayanımlı çeliklerin nokta direnç kaynaklanabilirliği ile ilgili bilimsel literatür incelendiğinde, bu prosesi tam olarak anlamak için ek çalışmalara ihtiyaç duyulduğu görülmektedir. Bu nedenle, bu çalışmanın motivasyonu ultra yüksek dayanımlı çeliklerde nokta direnç kaynağı hakkında nümerik ve deneysel yöntemlerle daha fazla bilgi edinmektir. Bu çalışmada, nokta direnç kaynak prosesinin sonlu elemanlar modeli MSC. Marc yazılımı ile eksenel simetrik ve elektrik-termal-mekanik birleştirilmiş bir model oluşturulmuştur. İş parçası olarak MS1500 ultra yüksek dayanımlı çelik seçilmiştir ve bu proses bu çalışmada aynı sac kalınlıklarındaki (1.2 mm) ve aynı malzemeden olan iş parçalarının birleştirilmesini içermektedir. Bu çalışma, sonlu elemanlar simülasyonu yardımı ile proses parametresi

olan akım değerlerinin varyasyonları için kaynak çekirdeğinin kalitesi, şekli, sıcaklık dağılımı hakkında bir tahmin sağlamıştır. İlk olarak, sonlu elemanlar yöntemi ile kurulan simülasyonların gerçek nokta direnç kaynağı prosesine yakınsaması için 8 kA ideal sinüzoidal alternatif akımla ve faz kaydırmalı alternatif akımla kurulmuş iki ana simülasyon oluşturulmuştur. Sonuç olarak kaynak süresi boyunca ideal sinüzoidal ile üretilen ısı miktarı, faz farklı akım ile üretilenden daha fazladır. Simülasyon sonuçları fiziksel deneylerle kıyaslandığında ise, nokta direnç kaynağı prosesinin sonlu eleman modelini oluşturmak için faz kaymalı akımla kurulmuş model tercih edilmiştir.8 kA faz farklı akımla kurulmuş simülasyonlar ile deneysel sonuçlar kıyaslandığında, son kaynak çevriminde çekirdek kalınlığında %40'lık, çekirdek çap uzunluğunda nispeten küçük %2'lik bir hata vardır. Deney sonucunda oluşan çekirdek şekli bir elipsken simülasyonda ise düz bir elipstir. Bundan sonra tüm simülasyonlar, farklı simülasyon modelleri için 7; 7,5; 8,5; 9; 9,5 ve 10 kA'lik faz farklı akım değerleri ile oluşturulmuştur. Simülasyon sonucuna göre faz farklı akım değeri arttıkça çekirdek çapı da artmaktadır. Ancak akım değeri arttıkça kaynak çevrimlerindeki enerji girdisi artığı için iş parçası /iş parçası ve iş parçası/elektrot arasındaki sıcaklık değerlerinde artış olmuştur. Sonuç olarak 8,5; 9; 9,5 ve 10 kA faz farklı akım ile kurulan simülasyonlarda elektrot ve iş parçası arasında malzeme ergimesi gözlemlenmiştir.

Anahtar Kelimeler: Nokta Direnç Kaynak, Ultra Yüksek Dayanımlı Çelikler, Kaynak Çekirdeği, Sonlu elemanlar analizi, MSC. Marc, Kaynak Çekirdeği Oluşumu, 1500M Martensitik Çelik

ACKNOWLEDGEMENT

TABLE OF CONTENT

LIST OF FIGURES

LIST OF TABLES

SYMBOLS AND ABBREVATIONS

Symbols

K   :   Kelvin Degree

MPa   :   Megapascal

kN   :   Kilonewton

kA   :   Kiloampere

K   :   Thermal Conductivity

V   :   Volt

 t   :   Time

°   :   Degree

Hz   :   Hertz

Abbreviations

MS1500   :   Martensitic Steel

RSW   :   Resistance Spot Welding

UHSS   :   Ultra High Strength Steel

HSS   :   High Strength Steel

AHSS   :   Advanced High Strength Steel

FE   :   Finite Element

FEM   :   Finite Element Model

FEA   :   Finite Element Analysis

AC   :   Alternative Current

Sec, s   :   Second

w.r.t : With Respect To

vs : Versus

SPFC : Specific Heat Capacity

1D : One dimension

2D : Two dimension

3D : Three Dimension

Inc : Increment

Weld. : Welding

Temp. : Temperature

Cyc. : Cycle

Nu. : Number

W/W : Workpiece/ Workpiece

W/E : Workpiece/ Electrode

1.INTRODUCTION

Technological developments in the 21st century provide the progress of many sectors such as production, construction, and automotive. As a result of the developing technology, many companies run against each other in many sectors. The existence of competition allows many companies to reach the customer for same scale products at a cheaper cost and in a shorter time. For example, when the production of a modern passenger car is considered, one of the used manufacturing methods is the welding methods. The RSW process, which is one type of permanent joining, is a preferable welding method for the automotive industry. The reason why the RSW process is preferred more than other welding techniques can be listed as follows: low cost, being faster than other welding methods, suitable for mass production [1]. These reasons, as mentioned above in the competitive environment, provide car manufacturers not only time saving but also low cost in the production of a modern passenger car. As a result, there are between 2000 and 6500 spot welds on modern passenger cars [2], from where it can be understood how substantial the RSW is for the automotive industry.

There are many investigations about simulation modeling of the RSW process in the scientific literature. Researchers have developed, 1D, 2D, and 3D predictive simulation models of the RSW process, via commercial software [3-18], and some of them focused on the joining of the mild steel materials, others on the joining of the advanced high strength steel materials. In this study, the RSW of the Ultra-high strength steel was examined with experimental and numerical methods. Over the past few years, there has been a significant increase in the use of UHSS in the automotive sector. Contrary to this growth, there are some challenges about UHSS. One of them is that there is no standard for joining of UHSS through RSW process. Secondly, lack of the scientific literature about UHSS, so additional studies to understand the resistance spot weldability of ultra-high-strength steel are needed. In this study, the resistance spot welding process of UHSS is examined to get more information through numerical, and experimental methods.

This study has been examined including the introduction part the following main headings which are state of the art, motivation, and method, finite element simulation model, results and discussion, as well as summary and outlook, respectively. Information and literature review related to the RSW process and UHSS, especially MS1500, are included, moreover, the topic of Joule heating is covered in the state-of-the-art heading. It is covered under motivation and method heading, which methods and how motivation this study has been taken. Then, the Finite Element analysis procedure in MSC. Marc is outlined and all boundary and initial conditions, geometry & mesh, and material properties under the Finite Element simulation model heading were elaborated. The results of the generated simulation with different current values were compared and a comparison was made with the experimental results to determine the type of alternative current used in the simulation. In the last heading, there is an overview and a brief evaluation of all the steps of this study.

2.STATE OF THE ART

The Resistance Spot Welding (RSW) pertains to one of joining methods and enables to joining of metal sheets. Regardless of the fact that RSW is complicated welding type, it is preferable method due to advantages which are the low cost, being faster than most of the welding methods, and the suitability for mass-production. This process is used for welding of 0.5-3 mm thick sheets and is appropriate for the joining of different sheet thicknesses, dissimilar materials (mild steel, high strength, advanced high strength and ultra-high strength steels, aluminum, copper, magnesium as well as their alloys). Aerospace, medical and especially automotive appear in the sectors that prefer the RSW method [1]. There are between 2000 and 6500 spot welds on modern passenger cars, from here it can be understood how substantial the RSW is for the automotive industry [2]. In other words, the RSW process enables passenger cars to get involved in high production assembly, so the RSW process is preferred by the manufacturer because of satisfying the selection criterions and requirements of the automotive sector.

RSW process, compared with many other welding methods, has advantages that make it preferable and disadvantages that limit its use. To mention the advantages is no extra material to weld the workpieces is needed. Not only providing an opportunity of weldability of thin workpieces but also suitability for automation is utilities of the RSW process. Steel has become more preferable to other metals due to its weldability performance. On the other hand, measurement during the RSW process is beset with a problem due to the high magnetic field. Irregularities of the sharp end of the weld nugget may cause propagation of the crack. Electrode wear is observed due to fatigue [1].
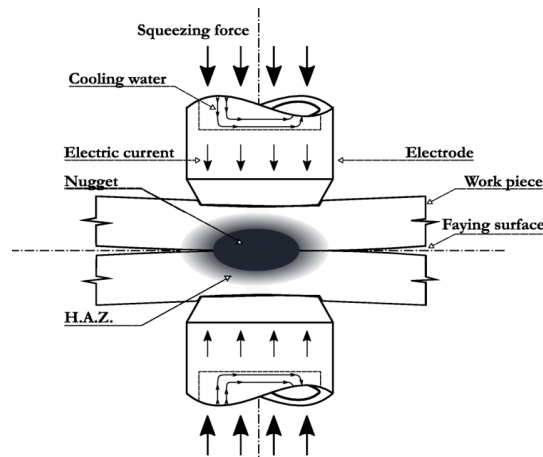
Figure 2. 1.Schematic of the RSW process [3]

Figure 2.1 shows the basic schematic of the RSW process and the physical mechanism of the RSW process can be described as follows, briefly: Workpieces are brought into contact with the force which was exerted by the upper copper electrode during squeeze time. Electric current movement from the upper electrode to the workpieces causes temperature rising at the faying surface during weld time and Joule law describes mathematically the heat generation at the faying surface in this stage.

$$Q = I^2\,RT$$

Where Q, I, R, T were the generated heat, the electric current, the sum of the resistances, and the welding current time in electric circuit, respectively. When the workpieces reach the melting temperature of the material, the nugget formation is observed at the faying surface. No electric current was applied during the holding stage and the force by exerted on the upper electrode is still active. The material shrinkage is observed after the cooling stage [1].
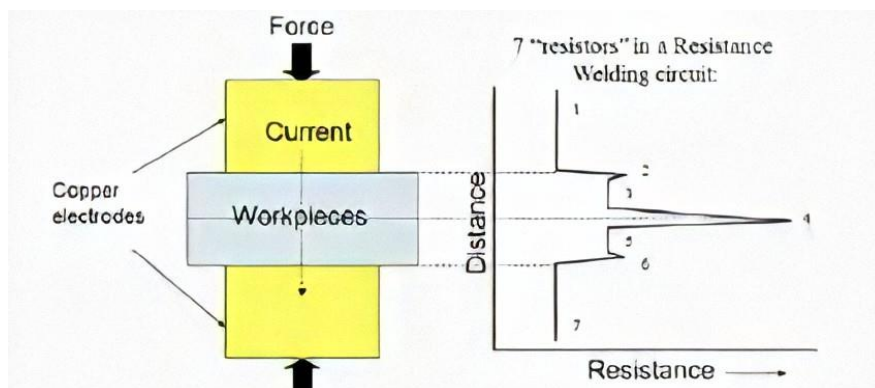
Figure 2. 2. Resistances associated with the RSW process [1]

One crucial point of the RSW process is contact resistances and bulk resistances. Those are depicted Figure 2.2. During welding time interval, resistors 1 & 7, resistors 3 & 5 represent the bulk resistance of the copper electrodes, and workpieces, respectively. Resistors 2 and 6, correspond the contact resistance between the electrodes and the workpieces, vary with temperature. Resistor 4 represents the contact resistance between the sheets interaction [1].

The RSW process is a permanent jointing process, and welding nugget size (nugget diameter and nugget depth) is a critical issue to check the welding quality. Many process parameters affect the welding quality. These parameters are related to the electrical, mechanical, thermal properties of the workpieces, and electrodes. Plastic-elastic region properties are related to mechanical properties of materials; latent heat properties, melting point, thermal expansion, heat conductivity, and specific heat capacity are related to thermal properties of materials. Electrical contact and bulk resistivity which are discussed above are electrical properties of materials. Electrode end shape as characteristic of welding equipment is important for weld quality. Electric current (applied current time, the current density, current type (DC & AC) is an important parameter for weld quality [4].

In the best-case scenario, the determination of the RSW process parameters is needed many physical experiments, which caused to increase experimental costs. Besides, it is difficult to make measurements under electromagnetic flux during the RSW process. Some of the tough challenges, and problems which all researchers encountered during the RSW physical experiment, are highlighted in the above section. Therefore, commercial software, which are ABAQUS, ANSYS, SYSWELD, became a popular tool to simulate the RSW process. There are many investigations about simulation modeling of the RSW process in the scientific literature. Researchers have developed, 1D, 2D, and 3D predictive simulation models of the RSW process, via commercial software [3-18]. When the benefits of the commercial software are considered, this study is intended the implicit finite element solver MSC. Marc software to construct an axisymmetric model of the RSW process using fully coupled electro-thermo-mechanical algorithms.

In 1984, Nied constructed an axisymmetric model via ANSYS code to simulate the RSW process in consideration of electrical, mechanical, thermal contact behaviours. Unlike other researches, this model included the electrode tip geometry effects (truncated and spherical end). Surface elements were defined to show clearly contact interaction between electrodes/workpieces in the FEM. The inclusion of the temperature-dependent properties of Type 321 austenite stainless steel (workpiece), and Class III type copper electrode was a crucial point for the simulation of this process. This investigation is important since it guided other investigations to build the finite element model, and Nied took aim at thermal deformation of workpieces. However, Nied did not take into consideration the plastic deformation of workpieces [4].

In 1997, Huh and Kang developed an axisymmetric finite element model of the RSW process to investigate the endurance of electrodes and welding quality. The simulation model with electrical thermal coupled was constructed to get temperature distribution results of electrode-workpieces assembly via finite element code. They took into consideration the contact resistance between electrode with elliptical-end and sheets, and interface elements were defined. The investigation results declared by this simulation as follows. The efficiency of the resistance spot welding was directly correlated with ellipticity of electrodes. Electric resistance between workpiece/workpiece had larger value than electric resistance between electrode/workpiece, and both values of resistances were affected negatively by temperature [5].

In 2000, Deng et al. developed a 3D finite element analysis model of the RSW process to expose mechanical behaviors of tensile-shear and symmetric-coach peel workpieces. The three-dimensional stress state was need-to-know point to analyze stress field around, and inside spot-welded via ABAQUS. At the end of this investigation, its results declared by this simulation as follows. One crucial point for the RSW process was the ratio between nugget diameter and thickness of the specimen when static load was applied, and failure occurred. If the nugget diameter is more or less than a certain value, the RSW fails due to fracture or rupture. Secondly, increasing of the thickness of one sheet specimen may affect implicitly the total strength of joints (assumed other conditions were the same) [6].

In 2003, B.H. Chang and Y. Zhou developed the axisymmetric finite element electrical-thermal and thermal-mechanical coupled models to investigate the electrode force effects on current density, and the temperature distribution between contact surfaces. This investigation was related to the small-scale RSW (SSRSW), which did not include a cooling stage (due to its limited electrode geometry). 1 kA direct current, and 50-100-150 kN force were applied to AISI 1008 steel sheets by the Class II type electrodes. Thermoelectric and isoparametric type solid elements were preferred for the thermal-electrical analysis, thermal-mechanical analysis, respectively. The potential of the bottom end of the lower electrode was set zero during electrical-thermal analysis. The electrode force at the lower value caused decreasing of the contact area. Temperature values at the faying surface began to increase more quickly on account of the decrease of the contact area [7].

In 2003, Wenqi Zhang exhibited research about how to design and execute the resistance welding process simulation through SORPAS software. The main target of the present paper was the adaptation of the resistance welding process into industry implementations, unlike other research papers. This paper showed that the batch simulation of this software can be simulated automatically by using a variety of process parameters [8].

Hou Zhigang et al. in 2006 focused on not only examining the thermal transient but also mechanical behavior of mild steel workpieces by using ANSYS software during the RSW process. A 2D axisymmetric RSW simulation model was composed of the thermal-electrical, and the thermo-elastic-plastic decoupled simulation models. Plane67, plane42 elements were added to the electrical-thermal, and the thermo-elastic-plastic coupled analyses, respectively. 50 Hz, and 12.2 kA sinusoidal current was applied to the top surface of the upper electrode. The weld time, and the hold time were 13 cycles (0.26 s), 3 cycles (0.06 s) respectively. The contact resistance value between W/W was assumed the function of temperature to construct the simple model. The simulation results were supported by the following statements: There was a relationship between temperature and the displacement of the upper electrode. The electrode displacement was monitored with the effect of thermal expansion, and shrinkage during the nugget formation. Electrode displacement has become an important parameter for process control of the RSW [9].

In 2007, Hou et al. generated a 2D axisymmetric thermo-elastic-plastic coupled FE model. The aim of this research was the detection of the contact pressure at the faying surface, and between workpiece/electrode interaction surface, stress-strain distributions on the welding field. Three different contact interfaces were defined interfaces between mild steel-workpieces/electrodes, and workpiece/workpiece, and sliding between these surfaces were permitted. 50 Hz alternative current was applied during 0.26 s weld time (13 cycles). Hold time, and electrode force were 0.06 s (3 cycles), and 3000 N, respectively. The inclusion of the latent heat of weld metal during phase transformation was a crucial point for the ANSYS simulation model. Hou et al. touched upon the significance of preventing liquid metal expulsion at the end of this investigation. High contact pressure at the outer boundary of the faying surface restrained the welding spatter. The contact pressure distribution between W/E contact area had a major effect on the endurance of electrodes. The contact area between workpieces was assumed to remain constant since the contact area between W/W changed about 0.5 mm when current was applied [10].

In 2009, H. Eisazadeh et al. worked on a 2D, thermal-electrical-mechanical coupling model with cylindrical coordinates to simulate a finite element model via ANSYS software. Nugget size and shape are important parameters, which exhibited the quality of the RSW process. The temperature-dependent properties of the AISI 1008 steel-workpiece, and copper-electrodes were defined to get the more accurate simulation analysis result. Simulation consisted of mechanical analysis (one load step), welding stage (23 load steps). During the squeeze stage of the RSW process, the different electrode forces were applied by the top electrode, and stayed constant during welding, and holding stages. The electric current fixed zero during the holding stage. At the end of the cooling stage, material shrinkage and electrode force affected the final nugget size. Finite element simulation results were supported by published experimental results (early-stage article), which were as follows. Firstly, there is an inverse correlation between nugget size and electrode force because of increasing the contact surface area by electrode force. Secondly, the maximum Von-Mises stress value belonged to the edge between the contact surfaces of W/E after the squeeze cycles [11].

In 2010, Thakur A.G. et al. worked on a 2D axisymmetric FE model to simulate the thermal behavior of the RSW process. The coupled structural-thermoelectric analysis model was simulated by using PLANE223 advanced coupled element of ANSYS software, and contact elements were CONTA172 and TARGE169. The main target of this investigation was the optimization of the RSW process parameters to become less the number of experiments. The contact resistivity value of W/W was regarded as the function of temperature. The temperature reached a maximum level at the center of the faying surface during the welding stage, and nugget formation was observed 10th cycle when the temperature reached the melting point of mild steel. The residual stress was seen inside the weld joint. After the welding stage, the temperature decreasing was observed owing to heat loss [12].

In 2012, R. Hashemi et al. has modeled and analyzed a 2D axisymmetric coupled electro-thermal-mechanical model to investigate the RSW process via ANSYS software. The mechanical model intended to investigate strain-stress distribution during the squeeze cycle of the RSW process. The decoupled electro-thermal model simulated to get results about the temperature field and the electrical voltage distribution. These results from this model used as the input parameter for the decoupled thermal-mechanical model. The thermo-mechanical model simulation results provided input for the electro-thermal analysis up to the end of the welding cycle. Finite element simulation results of AISI 1008 steel workpieces were supported by experimental results. These results gave the related information about the RSW process as following: The most effective parameter for the nugget growth was welding current. Secondly, if the welding time increased, the heat transfer (or loss) to the surrounding will increase, and the nugget formation will be affected in a negative way due to this energy loss [13].

In 2013, M. Vural developed a 2D finite element model of the RSW process to investigate temperature distribution on the welding area, welding quality and finding optimization parameters via ANSYS. PLANE223 type axisymmetric elements, and a 2D cylindrical coordinate system were used for thermal-electrical-mechanical coupling FE modeling. 50 Hz -sinusoidal electric current applied the top surface of the upper electrode, and I_{RMS} rule was valid for the lower electrode. Misalignment between W/E was neglected.

External compression force in the squeezing step of the RSW process was applied, and electrical, thermal load were taken no notice. When the electric current was off during the hold stage, the temperature value remained stable at 1500 °C. The main reason for the above observation was latent heat which occurs due to phase transformation. A molten nugget began to take shape in the center of the workpiece/workpiece interface because maximum temperature is observed W/W area [14].

In 2014, Takaya Kobayashi and Yasuko Mihara analyzed a 3D axisymmetric coupled electrical- thermal -mechanical model via ABAQUS to investigate the nugget development of steel workpiece. Electrode, electrode/workpiece interface, and workpiece/workpiece interface were aligned concerning the thermal conductance magnitudes (electrode has the highest thermal conductance value than others and lowest value of thermal conductance belongs to steel/steel interfaces and steel workpiece). Electric resistances magnitudes in magnitude order were workpiece to workpiece interface, electrode-to-workpiece interface, and electrode. (Workpiece-to-workpiece surface and bulk resistivity of steel workpiece have the highest electric resistance value than others). The following statements were deduced from the results of this article. Residual stress was observed via the FE model outer boundary of the elliptic nugget shape. When input current was increased, nugget diameter, and penetration ratio tend to increase, however current density tends to decrease due to increasing of contact area [15].

M. J. Vardanjani et al. presented this research to compare and re-examine FEM studies of the RSW process up to 2016. They touched on the differences in the Finite element method (FEM), and the Finite difference method (FDM) in this paper. The FDM was used in early-stage articles, and the FDA splits solid or region into a finite number element. The FEM was used in recent stage articles; FEA consisted of nodes, which have different variables for each analysis problem. The following statements were deduced from the comparisons of the simulation and experimental results of articles. The coordinate axis and W/W contact surface properties in constructed simulation model caused errors between the real process and predictive model, and differences between results on articles from past years. Most of researchers preferred decoupled model rather than a fully coupling model [16].

T. Kik et al. who built a 2D RSW model via SYSWELD state-art-software in 2017, split into three phases (phases: squeezing, weld nugget formation, forging), different from other researchers. SYSWELD software provided users with an opportunity, especially when the parameters (thickness, electrode type, welding, and current frequency) were entered software, this software constructed its geometrical model of the RSW process. Simulation results gave information about strain distribution concerning the electrode type during the RSW process [17].

In 2017, Y. Lee et al. built a 3D finite element model of the RSW process to investigate welding nugget development, welding quality, and temperature distribution via ABAQUS software. Three-dimensional simulation model of SPRC 340 steel-workpieces was constructed to get a more realistic study. During the RSW process, phase transformation with latent heat of weld metal was taken into consideration. The whole RSW process consisted of 4 stages, which are squeeze, weld, hold, and off. Electric field, and elastic-plastic analyses were investigated by using a theoretical background. Nugget weld diameter was compared with the experimental result, and minimum-maximum welding nugget diameter errors were 0.44%, 3.80%, respectively. Although previous investigations about weld nugget development had gotten large numerical differences between experimental and simulation results (nugget size), this investigation got more accurate results [18].

"The name Ultra-high strength steels (UHSS) was reserved for tensile strength exceeding 780 Mpa" [1]. Figure 2.3. shows that UHSS boundary in terms of tensile strength and total elongation.
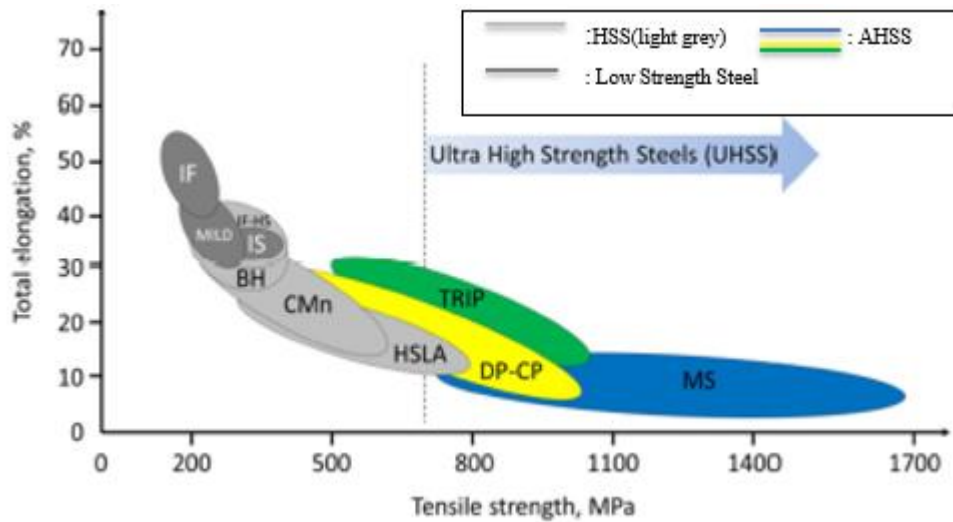
Figure 2. 3. Tensile Strength vs elongation graphics of steel types [1], [19]

Different joining methods can be used to weld the UHSS. Figure 2.4 displayed the comparison of the different welding methods for UHSS. The mechanical properties of welded UHSS are affected by different welding methods (These labeled methods are laser welding, gas shield arc welding, shielded metal arc welding methods, and plasma arc welding). Another joining method to weld the UHSS is the RSW process which is preferred welding implementation by the automotive sector [19].

	SMAW	GMAW	GTAW	LW
Process	Simple	Simple	Need skills	Accurate joint preparation is needed
Heat Input	Low	High	High	Low
HAZ	Relatively Small HAZ, low softening	May have wide HAZ and high softening	May have wide HAZ and high softening	Small HAZ, low softening
Welded joint properties	-	Good strength and plastic properties is possible	Good strength and plastic properties is possible	Good strength, but poor bending properties may occur

Figure 2. 4. Comparison of various welding methods to weld the UHSS [19]

Ultrahigh strength steels especially fulfill the expectations of the automotive sector, which are the increased crashworthiness, fuel efficiency combined with light weight. For example, the usage areas of HF steel on the automotive sector are A- and B-pillars, sidewall members. Volvo preferred to use HF Boron steel in its 2010 model C70 passenger cars before usage of UHSS become familiar [20]. In recent years there has been considerable growth of using the AHSS and UHSS in the automotive sector. B-pillar,

frame rail of 2019 model SUBARU Forester body is made of 56 percent High-strength-steel. The body 2019 model JEEP Cherokee consisted of high strength, hot-stamped steels, and UHSS (as 65 percent). 2020 model TOYOTA Corolla is used ultra-high-strength steels to increase the crashworthiness [21].

Many researchers have purposed to analyze the RSW process via commercial software, and some of them focused on the joining of the mild steel materials, others on the joining of the advanced high strength steel materials. Additional studies to understand more completely the resistance spot weldability of ultra-high-strength steel are needed, due to lack of the scientific literature about UHSS. Therefore, the motivation of this study is to get more information through numerical, and experimental methods about the resistance spot welding process of UHSS.

In 2012, W. Zheng et al. worked on a coupled-axisymmetric FE model to simulate the RSW process by using SORPAS software. Hot-stamped UHSS (BR1500HS-UHSS-Usibor1500) and mild steel (HC260LAD) were used as workpieces. The aim of this investigation was analyzing the scattering of welding and highlighting the temperature distribution around the welding field. 1 cycle for simulation was regarded as 20 ms, and squeezing time was defined 15 cycles. Three different simulation parameters which displayed the given below in Figure 2.5, were used to find out the optimum parameter of UHSS, and mild steel during the welding stage. The maximum temperature was observed at the center of the welding nugget for all cases (1.1-1.3) [22].

No.	Current pulse	I_1(preheat)/kA	I_2(weld)/kA	I_3(temper)/kA
1-1	Monopulse	–	9.97	–
1-2	With preheated	10.08	9.97	–
1-3	Triple-pulse	10.12	9.96	10.12

Note: weld time t_1(preheat)=t_2(weld)=t_3(temper)=6 cyc

Figure 2. 5.Welding parameters for different current pulse [22]

Weld nugget of the UHSS side formed beforehand than the mild steel side and there were heating rate differences in the two dissimilar materials. At the end of the simulations,

simulation results were compared with experimental results. The big welding spatters was observed in all different experimental case. Nugget size in the simulation results was seen a little bit different than experimental nugget size because the loss of nugget depth. The UHSS side was twice as many nuggets welding size as mild steel side. And then, RSW process simulation parameters were readapted to minimize experimental cost. The preheating current value was modified to prevent the scattering of welding and the modified welding parameter displayed the following Figure 2.6 [22].

No.	I_1(preheat) kA	I_2(weld) kA	I_3(temper) kA	t_2(weld) cyc	t_3(temper) cyc	Current pulse
2-1	3.96	9.90	–	15	–	With preheated
2-2	3.95	9.88	6.08	15	10	Triple-pulse

Note: Weld time: t_1(preheat)= 6 cyc; weld current: $I_1 \approx 40\% I_2$, $I_3 \approx 60\% I_2$

Figure 2. 6.Welding parameters for different current pulse [22]

The weld quality of No. 2-1 was better than No. 2-2, so parameter No. 2-1 was chosen as an optimum case, and scattering of welding in 2-1 case was prevented [22].

In 2014, O. Andersson et al. developed an axisymmetric electro-thermal-mechanical-metallographically coupled FE model to investigate the welding spatter phenomena, welding quality (nugget shape and size), and finding optimization parameters for the RSW process. Six steel materials (BO1500, RP260, DP600, DP800, DP1000, MS1400) whose yield strengths were from 260 Mpa to 1500 Mpa, were used as workpieces to analyze during the RSW process, and two welds applied for each sheet pair. Hooke's law was used for modeling of elasticity region, and Hollomon's curve was used to model the plastic region. Johnson-Mehl-Avrami's transformation was used to model the metallurgical transformations. This process was simulated through SYSWELD software, and simulation, and experimental results were compared. The welding parameters displayed as below figure. Coach peel test was applied to check the welding quality and welding size [23].

Material	Weld time [ms]	Electrode force [kN]	Hold time [ms]	Minimum weld current [kA]	Maximum weld current [kA]
BO1500	330	3.6	150	5.0	10.1
RP260	400	4.5	150	6.0	9.9
DP600	340	4.1	150	6.6	10.2
DP800	330	3.8	150	7.2	9.9
DP1000	400	4.0	150	6.6	9.0
MS1400	350	4.1	170	6.7	10.0

Figure 2. 7. Process parameters of experimental welding [23]

At the end of experimental and simulation results, the shunting effect was not included in FE simulations because of a lack of FE software capability. The importance of advance module for materials properties was highlighted because behaviors of steel in molten, and pressure state were important for predicting expulsion statement. The nugget size of the second weld is lower than the first weld in the experiment due to the shunting effect [23].

In 2015, Y. Zhishui et al. focused on the weldability of hot-formed UHSS (B1500HS), and B250P (cold rolled commercial steel) workpieces. A 2D axisymmetric RSW model was generated by using SORPAS and constructed with thermal-mechanical-electrical coupling. Shear tension and cross-section test was applied jointed workpieces to check the welding quality. Electrode force, squeezing, and hold time were 3.5 kN, 30 cycles, and 15 cycles, respectively. These parameters were used as constant parameters, and two different welding currents were applied as 9.5, 12.5 kA. The other variable parameter was welding time (8 and 16 cycles). The results of this study were reported as follows. When the Heat Affected Zone (HAZ) size enlarged, the nugget size could increase up to a certain level. After that point, the increasing rate began to increase slowly [24].

In 2017, Demir et al. presented the experimental results of two AHSS workpieces (DP 800 and TRIP 800) during RSW process in this paper. Shear test was applied to these workpieces, and nugget development between the sheets was measured through Clemex Programme. The thickness of the sheets, and current density were changed to create different combination for experiments. Experimental results showed that nugget weld diameter increased due to the increase of current density. Microstructural examination showed that columnar appearance in DP steels were more dominant than TRIP steels one,

under 5kA current density owing to high Mn of DP steel composition. TRIP 800 test samples exhibited a different fracture property than DP 800 steels in the shear test [25].

In 2017, Wan et al. focused on the stress-strain distribution of Dual-Phase steel (DP600) workpiece via numerical simulation software. A 2D axisymmetric RSW model was generated with thermal-mechanical-electrical coupling, and experimental results were consistent with ANSYS simulation results. During the RSW process, 3.5 kN electrode force and 10 kA were applied. During welding stage, nugget development was not observed up to 0.08 s through simple thermal electrical analysis. The peak value of the current density was positioned at the edge of the zone of the sheet/electrode contact area, and the current density at the faying surface declined to zero value when it went far away from the weld center. When temperature reached the melting point, nugget development gained momentum. After that, when the welding time increased because of heat dissipation (due to water cooled by electrode), nugget development velocity decreased. A simple thermal-mechanical model was used for contact radius detection during the squeezing time. At the end of the simulation, simulation results demonstrate that the contact area during the squeezing stage is unrelated to force [26].

3.MOTIVATION AND METHOD

Many researchers aimed to analyze the RSW process via commercial software, and some of them focused on the joining of the mild steel materials, others on the joining of the advanced high strength steel materials. Further studies are required to more fully understand the point of weldability of the UHSS because of the lack of scientific literature on UHSS. The reason for this study is therefore to obtain more information through numerical and experimental methods on RSW process of the UHSS. This study includes an examination of the resistance spot welding process of the ultra-high-strength steel (MS1500) with experimental and numerical methods. MSC. Marc software was used to construct an axisymmetric model of the RSW process. The FE model was built as electrical-thermal-mechanical coupled. This model makes it possible to represent the interaction between mechanical, electrical, thermal phenomena. This study aims to the convergence of the Finite Element (FE) models for the real RSW process by comparing simulation results to physical experiments**.** The RSW process simulation through MSC. Marc software aims the investigation of the process aspects in more detail. The numerical method provides adjusting of welding parameters, decreases the number of experiments. The other aim of this study is the determination of optimization value for the RSW process by using the results of FE analysis. The nugget quality and shape indicate the RSW process quality, so the prediction of the nugget development during this process is important. One target of this study provides a prediction shape and dimension of the weld nugget for process parameters, which are AC type, AC values, and also the simulation results should be in agreement with experimental results.

4.FINITE ELEMENT SIMULATION MODEL

In this study, the finite element (FE) model of the RSW process was modeled via MSC. Marc 2016.0 software. FE modeling of the RSW process in MSC. Marc consists of pre-processing, processing, and post-processing sections. Figure 4.1 shows the FE analysis procedure. The FE model of the RSW process was generated as fully electrical-thermal-mechanical coupled. In this part of this thesis, axisymmetric model generation procedure is demonstrated.
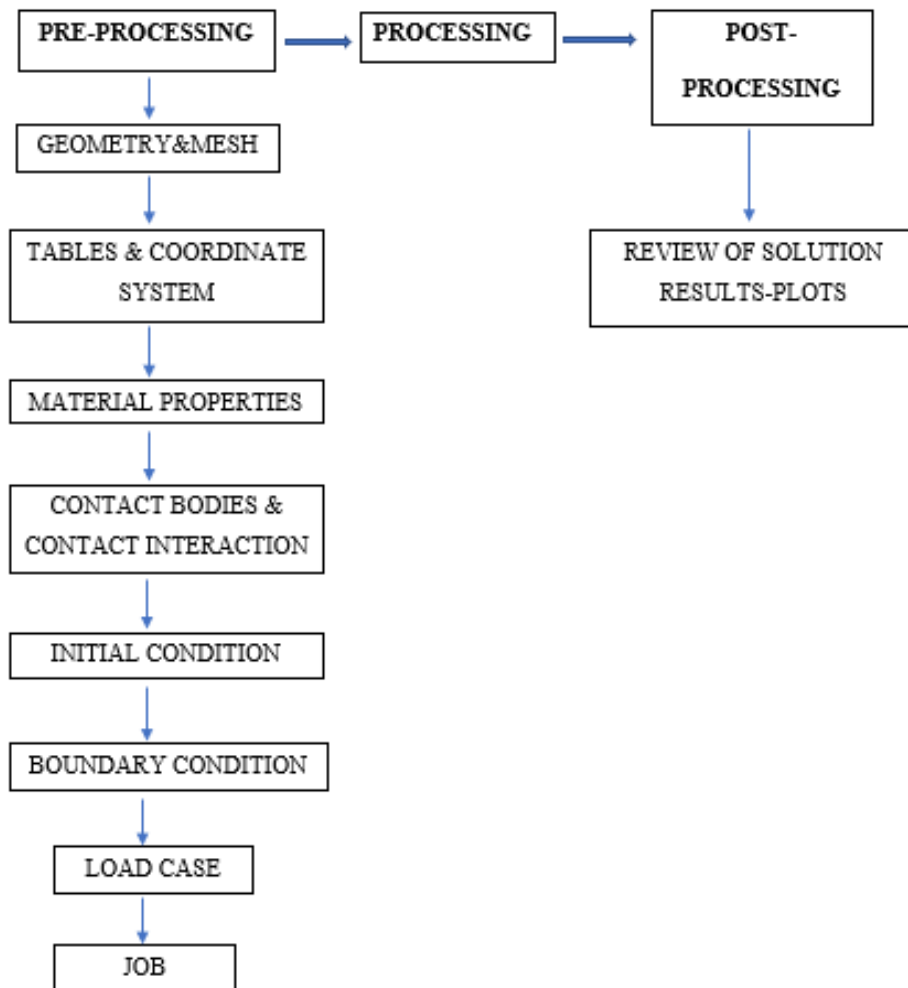
Figure 4. 1.The Finite Element Modeling Procedure in MSC. Marc

At the beginning of the finite element model generation, the units of the material properties to be used in simulations was determined. Table 4.1 depicts units of the material properties for MSC. Marc software.

Table 4. 1. Units of the Material Properties in MSC. Marc

PROPERTIES	UNITS
Temperature	Kelvin
Length	Millimeter
Density	Mg/mm^3
Mass	Mg
Stress	MPa
Current	Ampere
Thermal Conductivity	N/sec/K
Electrical Contact Resistivity	$\Omega.mm^2$
Electrical Bulk Resistivity	$\Omega.mm$
Electrical Contact Conductivity	$1/(\Omega.mm^2)$
Electrical Conductivity	$1/(\Omega.mm)$
Specific Heat Capacity	$mm^2/sec^2/K$

Electrode modeling strategy must be decided before constructing the simulation geometry model. Electrodes can be modeled in three different ways for finite element analysis. These are the rigid geometric, the rigid meshed, or the deformable meshed bodies. The deformable meshed body allows stress, and temperature distribution on electrode but if the electrode is designed as a deformable meshed body, the young modulus value of the copper electrode must be high. Secondly, the rigid geometric model allows heat transfer, but a constant temperature can be defined on the curve. On the other hand, the rigid meshed model allows heat transfer and temperature distribution. Considering all stages of the RSW process, the temperature distribution on the electrode is observed. The copper electrode is exposed to different temperatures during the cooling stage and also copper electrode has the thermal conductivity coefficient. Therefore, the rigid meshed model for the electrode modeling strategy was preferred. So, during the construction RSW simulation model, the electrode geometry was modeled as rigid and divided into nodal elements. Figure 4.2 shows schematically the differences between the rigid-geometric electrode model and the rigid-meshed electrode model.
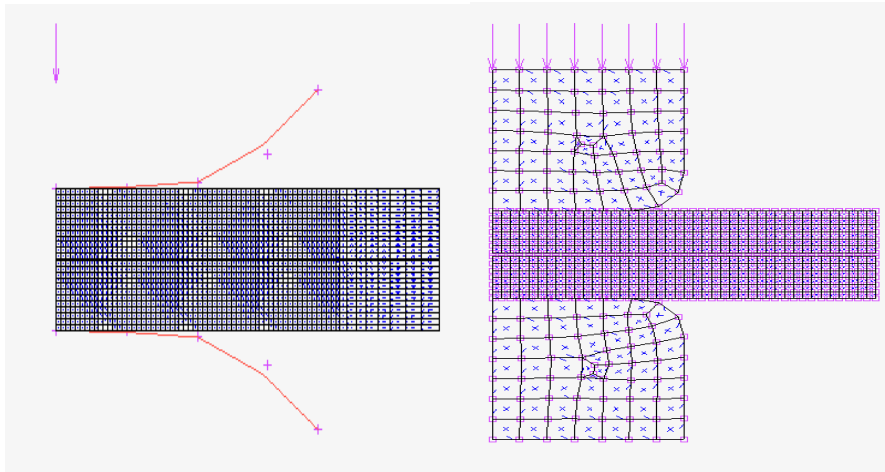
Figure 4. 2.The Comparison of Rigid-Geometric, and Rigid- Meshed Electrode Model

In the geometry & mesh subsection of pre-processing, electrode and sheet geometries were created, and quad-meshed type was chosen for electrode, and workpiece meshing. In this FE model, the x-axis was the axisymmetric axis, and the upper electrode can proceed to x displacement. Firstly, a 3 mm spherical-end electrode model was drawn in RSW model generation. The thicknesses and lengths of MS1500 sheets workpieces were 1.2 mm, 8 mm, respectively. The distance between the sheets was 0.1 mm in the FE model. There is no distance between the upper electrode-upper workpiece and the lower electrode-lower workpiece. The FE model of the RSW process consisted of 738 nodes and 612 elements. The element lengths for sheets were 0.1906 mm in the u direction and 0.2 mm in the v direction, which was shown clearly in Figure 4. 3. The coarse mesh elements for electrodes were preferred, and the length of elements was 0.6 mm.
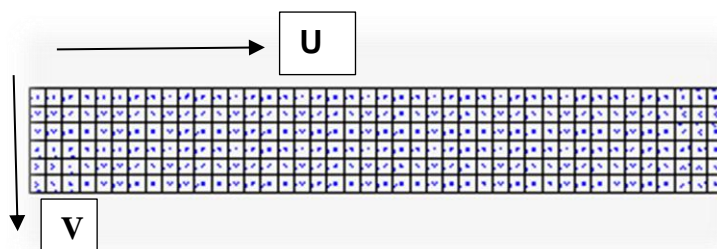
Figure 4. 3.Meshing of MS1500 workpiece

The tables & coordinate system section of pre-processing part enables to have entered the material properties value concerning to independent variables. Material of the workpiece, and electrodes are MS1500 (UHSS), CuCr1Zr, respectively. Figure 4.4 shows the material properties of workpieces and electrodes, and Table 4. 2 indicates the MS1500 chemical composition.
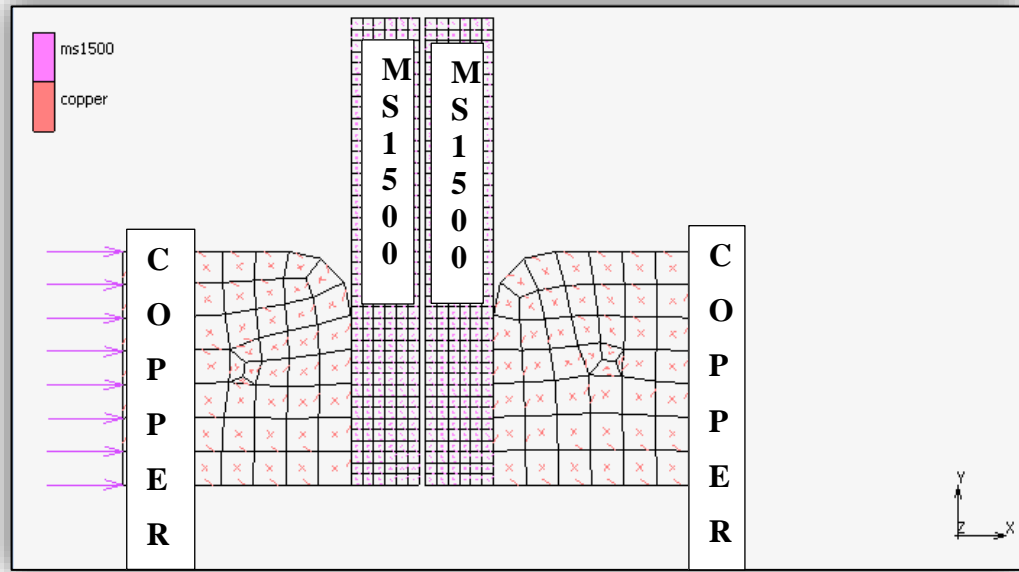
Figure 4. 4.Materials of Workpieces and Electrodes in FE Model

Table 4. 2.　MS1500 Chemical Composition (%) [27]

	C (max %)	Si (max %)	Mn (max %)	P (max %)	S (max %)	Al (min %)	Nb+Ti (max %)
MS1500	0.28	0.40	1.30	0.020	0.010	0.015	0.10

Electrical-thermal-mechanical coupled simulation model provides modeling of the interaction between mechanical, electrical, thermal phenomena [18]. The mechanical model provides calculation of deformation, stress, and strain distribution of the workpieces, the temperature field is needed to determine material temperature-dependent

properties. The electric model calculates heat generation source and current distribution, so thermal, mechanical, and electrical properties of MS1500, and copper were defined in this material properties heading. Mechanical properties of MS1500 were defined as isotropic elastic-plastic material. Johnson Cook method was chosen to define the plasticity properties of MS1500. The rigid-plastic model type was used for the copper electrode. Table 4.3 shows Young modulus, Poisson's ratio, mass density, and the Johnson-Cook material parameters of MS1500.These table entries were derived from experimental results. Table 4.4 indicates the mass density value of the copper electrode.

Table 4. 3.   Johnson-Cook material model parameters for MS1500

Parameter	MS1500
Mass Density [Mg/mm^3]	$7.85*10^{-9}$
Young's Modulus [GPa]	205
Poisson's Ratio	0.29
A – Yield Stress [MPa]	1310
B – Strain Hardening Constant [MPa]	224.8
N – Strain Hardening Coefficient	0.08
C – Strengthening Coefficient of Strain rate	0.01
$\dot{\varepsilon}_0$ – Reference Strain Rate [s^{-1}]	1
T_0 – Room Temperature [K]	298
T_m – Material Melting Temperature [K]	1689
m – Thermal Softening Coefficient	0.6

Table 4. 4.   The Mass density value of copper electrode [9]

Parameter	Copper Electrode
Mass Density [Mg/mm^3]	$8.9*10^{-9}$

The heat transfer is the crucial point of the RSW process, so the materials thermal properties of copper and MS1500 must take into consideration. Thermal conductivity and specific heat capacity values of materials were shown in tabulated format and graphically. Table 4.5 and Table 4.6 indicate the specific heat capacity value of MS1500 and copper

electrodes, respectively. Specific heat capacity value of copper electrode was taken from the literature [9] which was shown in Figure 4.5 and the specific heat capacity tabulated values of MS1500 were gotten from the educational package of Thermo-Calc software, in which users can define the chemical composition of materials up to 3 elements. % 98.5 Fe, %1.25 Mn, and % 0.25 C elements with the highest percentage in MS1500 were chosen to calculate the specific heat capacity value of MS1500. Additionally, the specific heat capacity value does not calculate directly in the software interface, so function which is derivative of enthalpy with respect to the temperature was defined in the software interface. When Figure 4.6 is examined in detail, a peak about 1003 K is seen due to the carbon content of most carbon steels, because of chemical transformation from ferrite-pearlite to austenite in this temperature [18]. The second peak in Figure 4.6 shows that the specific heat capacity value increased up to 1700 K and then stay constant during the phase changing of MS1500. Latent heat phenomena describe keeping the temperature constant during phase changing.

Table 4. 5.   The Specific Heat Capacity of MS1500

Temperature (Kelvin)	SPFC*$10^9 \frac{mm^2}{K.sec^2}$	Temperature (Kelvin)	SPFC*$10^9 \frac{mm^2}{K.sec^2}$
275	0.436	1773.75	6.457
411.25	0.498	1970.75	6.457
547.5	0.566	2046	0.827
683.75	0.64	2182.5	0.828
820	0.744	2318.75	0.828
956.25	0.925	2455	0.828
1092.5	0.598	2591.25	0.828
1228.75	0.619	2727.5	0.828
1365	0.64	2863.75	0.828
1501.25	0.661	3000	0.828
1637.5	0.683		

Table 4. 6. The Specific Heat Capacity (SPFC) of Copper[9]

Temperature (Kelvin)	SPFC*$10^6 \frac{mm^2}{K.sec^2}$	Temperature (Kelvin)	SPFC*$10^6 \frac{mm^2}{K.sec^2}$
294	397.8	700	439.6
366	401.9	811	452.2
477	418.7	922	464.7
589	431.2	1033	473.3
		1477	502.4
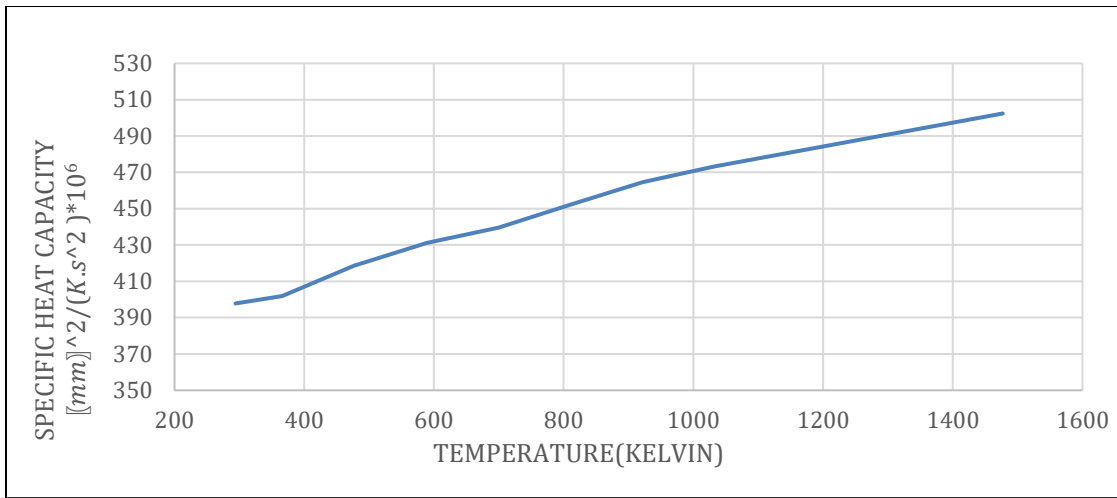
Figure 4. 5.The Specific Heat Capacity Values of Copper Electrode w.r.t Temperature
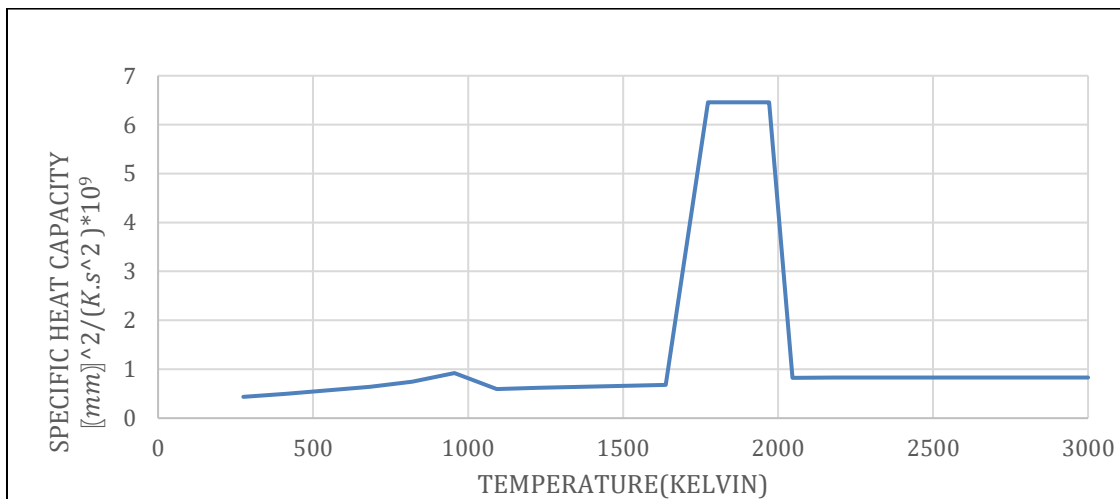
Figure 4. 6.The Specific Heat Capacity Value of MS1500 w.r.t Temperature

The thermal conductivity values of MS1500 and copper were shown in tabulated format. The thermal conductivity value of copper was taken from the literature [9]. Researchers adhered to results from numerical, and thermodynamics software to find the thermal conductivity value of MS1500 due to experimental incompetence and difficulty in measuring under high electromagnetic flux during the RSW process. But there is noncoincidence in scientific information about the thermal conductivity value of Martensitic Steels in the literature. Wang et al [28] used the thermal conductivity value of M1500 which decreased up to 900 Kelvin and then increased with temperature. Andersson et al. [23] used the thermal conductivity value of MS1400 which decreased with increasing temperature. In this thesis, the thermal conductivity value of MS1500 was assumed to decrease with temperature and the thermal conductivity value of MS1400 was used [23]. Table 4.7 and Table 4.8 indicate the thermal conductivity of the copper electrode, and MS1500, respectively.

Table 4. 7.   The Thermal Conductivity of Copper [9]

Temperature (Kelvin)	[K] Copper Thermal Conductivity (N/sec/K)	Temperature (Kelvin)	[K] Copper Thermal Conductivity (N/sec/K)
294	390.3	922	320
366	380.6	1033	315.5
477	370.1	1144	310.3
589	355.1	1255	305
700	345.4	1366	300.1
811	334.9		

Table 4. 8.   The Thermal Conductivity of MS1500 [23]

Temperature (Kelvin)	MS1500 Thermal Conductivity (N/sec/K)
294	51.55
473	48.89
773	47.16
973	46.29
1173	45.24
1373	44.26
1743	43.55
1828	42.16
2273	41.64

The thermal expansion coefficients of MS1500 and Copper were shown in tabulated format. The thermal expansion coefficient of copper was taken from the literature [9]. Table 4.9 and Table 4.10 show the thermal expansion coefficient of MS1500 and copper electrode, respectively.

Table 4. 9.   The Thermal Expansion Coefficient of MS1500

Temperature (Kelvin)	The Thermal Expansion Coefficient of MS1500 (1/Kelvin)
1300	$2.46 * 10^{-6}$
1500	$1.00 * 10^{-6}$

Table 4. 10.   The Thermal Expansion Coefficient of Copper Electrode [9]

Temperature (Kelvin)	The Thermal Expansion Coefficient of Copper Electrode (1/Kelvin)
294	$1.656*10^{-5}$
366	$1.674*10^{-5}$
477	$1.710*10^{-5}$
589	$1.746*10^{-5}$
700	$1.782*10^{-5}$
811	$1.836*10^{-5}$
922	$1.854*10^{-5}$
1033	$1.890*10^{-5}$
1144	$1.926*10^{-5}$

The electrical bulk resistivities of copper, and MS1500 are another important parameter of the RSW process. In this work, no experimental studies have been done for measuring electrical and contact resistances due to difficulty in measuring under high magnetic flux during the RSW process and lack of experimental equipment. Electrical bulk resistivity value of 4140 steel from literature was handled due to similarity of MS1500 chemical contents [29]. Table 4.11 depicts the electrical resistivity of MS1500. The bulk electrical resistivity value of copper electrode which was obtained from the literature [9] was depicted below in Table 4.12.

Table 4. 11.   MS1500 Bulk Electrical Resistivity [29]

Temperature (Kelvin)	MS1500 Electrical Resistivity (Ω.mm)	Temperature (Kelvin)	MS1500 Electrical Resistivity (Ω.mm)
293	$1.93*10^{-4}$	1873	$1.78*10^{-3}$
373	$2.38*10^{-4}$	2123	$2.004*10^{-3}$
473	$3.05*10^{-4}$	2373	$2.17*10^{-3}$
673	$4.69*10^{-4}$	2623	$2.257*10^{-3}$
873	$6.64*10^{-4}$	2873	$2.248*10^{-3}$
1123	$9.38*10^{-4}$	3123	$2.123*10^{-3}$
1373	$1.228*10^{-3}$	3373	$1.864*10^{-3}$
1623	$1.515*10^{-3}$	3623	$1.452*10^{-3}$

Table 4. 12.   Bulk Electrical Resistivity for Copper [9]

Temperature (Kelvin)	Copper Electrode Electrical Resistivity (Ω.mm)
294	$2.64*10^{-5}$
366	$3.00*10^{-5}$
477	$4.00*10^{-5}$
589	$5.05*10^{-5}$
700	$6.19*10^{-5}$
811	$6.99*10^{-5}$
922	$8.00*10^{-5}$
1033	$8.98*10^{-5}$
1144	$9.48*10^{-5}$
1255	$9.98*10^{-5}$

In the contact bodies section, elements of the upper electrode, lower electrode, upper workpiece, and lower workpiece (sheet) were defined separately and the contact bodies in the FE model was shown in the Figure 4.7. In contact section parts, contact interactions, and contact table enable users to determine potential interaction between bodies. Upper and lower sheets were modeled as meshed (deformable) bodies because this type of body allows becoming deformed and show temperature and stress distribution. Lower, and upper electrodes were modeled as meshed (rigid) bodies.
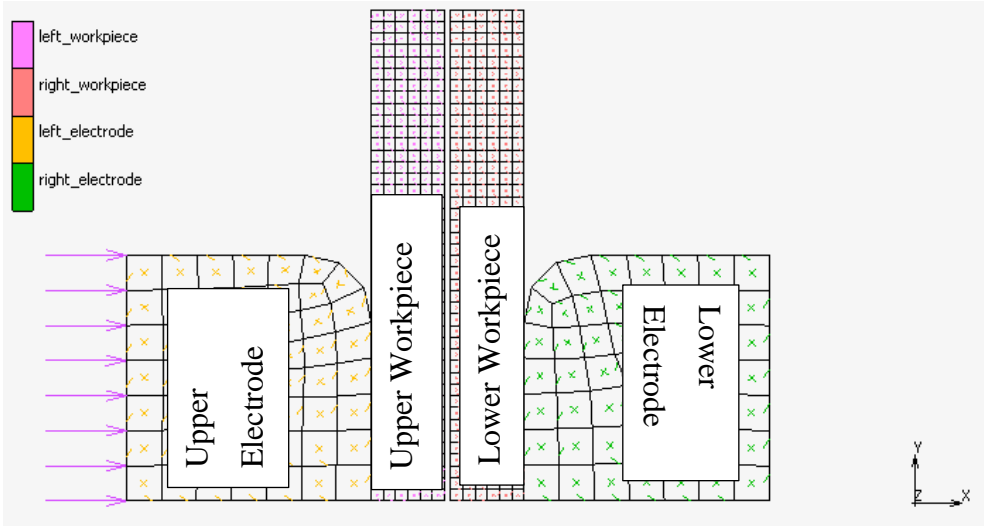
Figure 4. 7.The Contact Bodies in The Finite Element Model

The structural boundary conditions were defined contact bodies heading but there is a deficiency about body control of the rigid-meshed body in MSC. Marc. The rigid-meshed model of the upper electrode is not allowed to control by load or force. There are options to control the rigid body by load, velocity, or position but load control is not supported by the MSC. Marc interface. Since this problem is encountered, the upper copper electrode is controlled by displacement. Figure 4.8 shows the displacement of the upper electrode in x-axis during the RSW process time. The displacement of the upper electrode between 0.2- 0.4 seconds was constant and 0.101 mm.
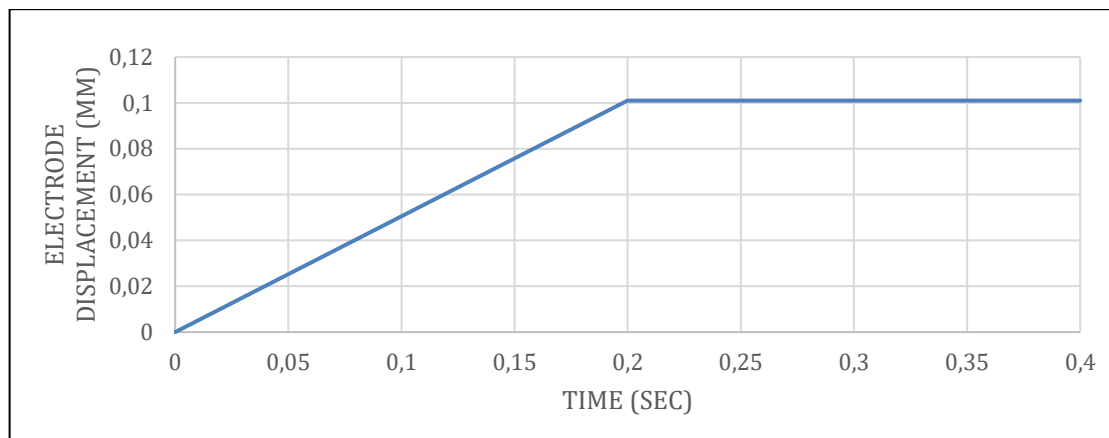
Figure 4. 8.Displacement of the Upper Copper Electrode in x direction

Electrode modeling strategy was declared in the previous paragraph. In this FE model, there are two different type interactions that are workpiece-to-workpiece (W/W), and workpiece-to-electrode (W/E). Workpiece-to-workpiece, and workpiece-to-electrode contact interaction types were meshed (deformable) versus meshed (deformable), meshed (deformable) versus meshed (rigid), respectively. The mechanical, electrical, and thermal properties of these interactions were defined in this part of the simulation. The electrical contact conductivity values of W/E and W/W are key parameters of the RSW simulation model which have been entered to change with temperature in Figure 4.9 and Figure 4.10. Table 4.13 and Table 4.14 show the contact conductivity values of W/E and W/W, respectively.

Table 4. 13. The Electrical Contact Conductivity of W/E

Temperature (Kelvin)	W/E Contact Conductivity $(1/(\Omega.mm^2))$	Temperature (Kelvin)	W/E Contact Conductivity $(1/(\Omega.mm^2))$
273	8	1573	66.7
673	10	1873	72
950	52	2273	81.3
1273	90		

Table 4. 14. The Electrical Contact Conductivity of W/W

Temperature (Kelvin)	W/W Contact Conductivity $(1/(\Omega.mm^2))$	Temperature (Kelvin)	W/W Contact Conductivity $(1/(\Omega.mm^2))$
273	9	973	9
373	9	1273	12.22
473	9	1573	15.38
573	9	1873	18.52
773	9	2273	30.25
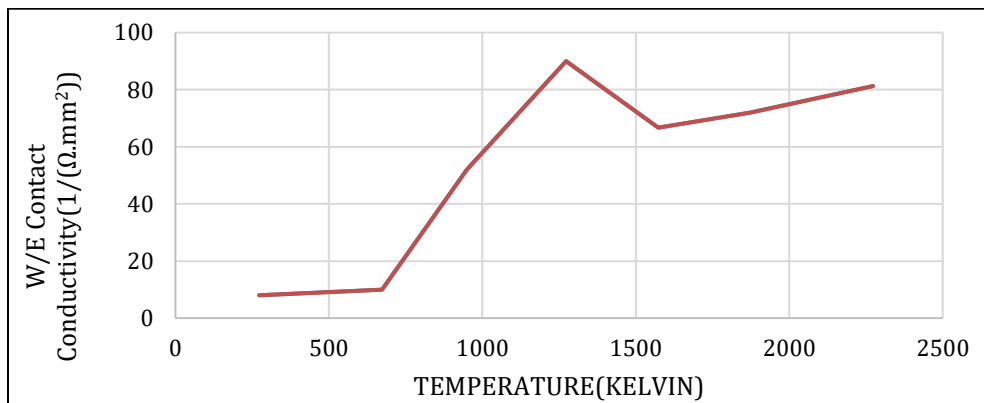
Figure 4. 9.W/E Contact Conductivity With Respect To Temperature
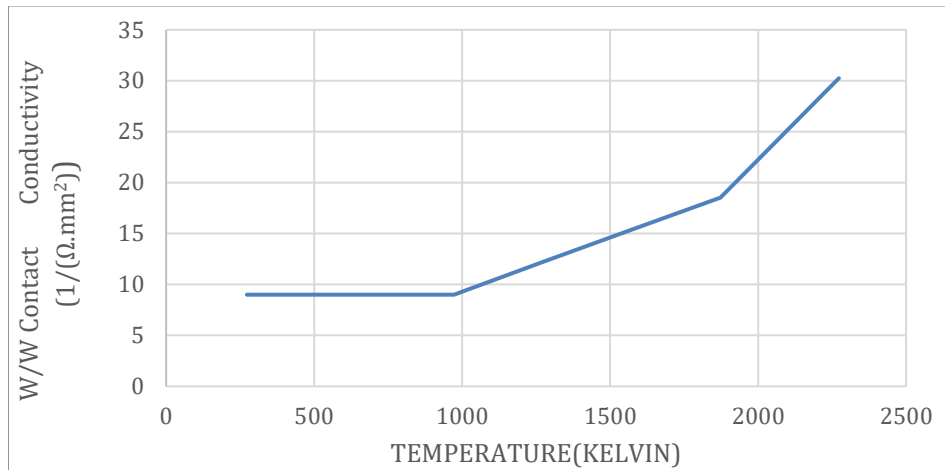
Figure 4. 10.W/W Contact Conductivity With Respect To Temperature
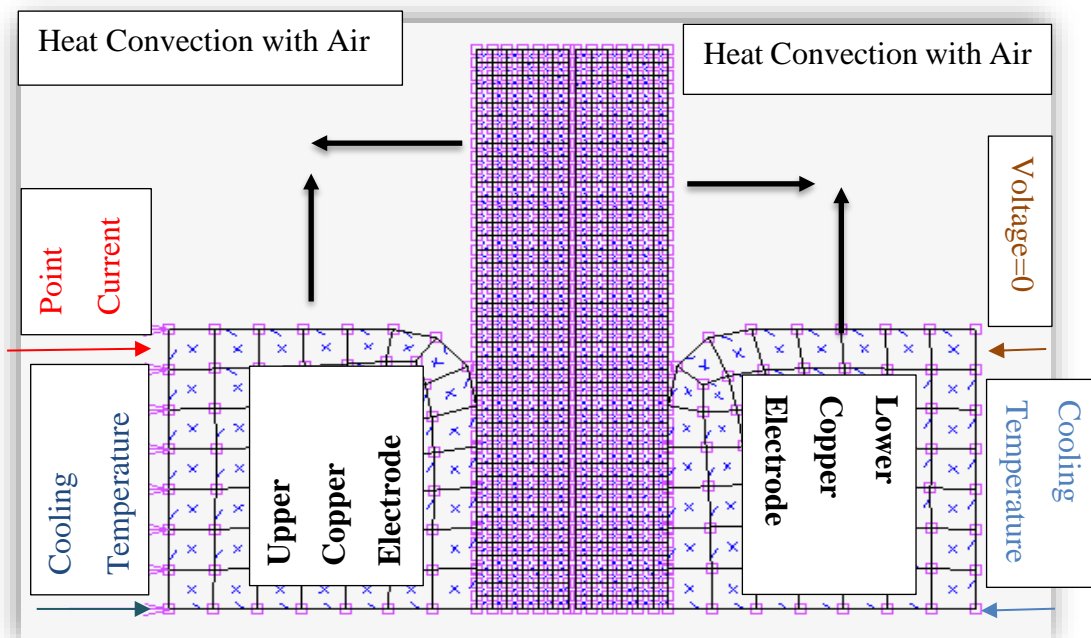
Figure 4. 11.The Boundary Conditions of the Finite Element Model

In Figure 4.11 the structural, electrical, and thermal boundary conditions are indicated. For the lower side of the lower electrode, electrical voltage is defined as zero (V=0). The cooling temperature is equal to 298 K which was applied upper side of upper electrode, lower side of lower electrode. Heat convection was defined for workpieces and electrodes. Table 4.15 depicts thermal constants of heat transfer to the environment. 298 K thermal temperature is applied for all nodes on electrodes and sheets (as an initial condition). The structural boundary conditions were defined beforehand under the geometry-mesh heading and no mechanical boundary condition was defined in this step

of the finite element model construction. To summarize the mechanical boundary condition, motion of the lower electrode was restricted to move x-axis, and the motion of the upper electrode was allowed to move along the x-direction. The motion in y axis of upper and lower electrodes is restricted to prevent slip on contact surfaces.

Table 4. 15.   Thermal Constants During Heat Transfer To The Environment

Heat Transfer Coefficients (N/m/sec)	0.021
Sink Temperature (Kelvin)	298
Natural Convection Coefficient	100
Natural Convection Exponent	1

An ideal AC and phase shifted current was applied on upper side of the upper electrode. The below formula was used for the ideal sinusoidal current calculation.

$$A(t) = \sin(2\pi ft)$$

In this function, t is welding time, and inside of the sine function must be in radian. f value equals 50 Hz because 50 Hz welding machine was used as welding equipment. 50 Hz depicted that 50 sinusoidal waves are observed in one second, so one cycle time calculated below.

$$1 \text{ cycle} = \frac{1}{50} = 0.02 \text{ sec}$$

An ideal sinusoidal electrical current graphics in Figure 4.12 was shown. The simulation models in which currents were applied as constant 8 cycles to be different welding current values. One of the simulation models was used 8 kA ideal alternative current value to compare the results of the simulation model which was applied a non-ideal 8 kA sinusoidal current (phase shifted AC) which consisted of 8 cycles (0.16 s).
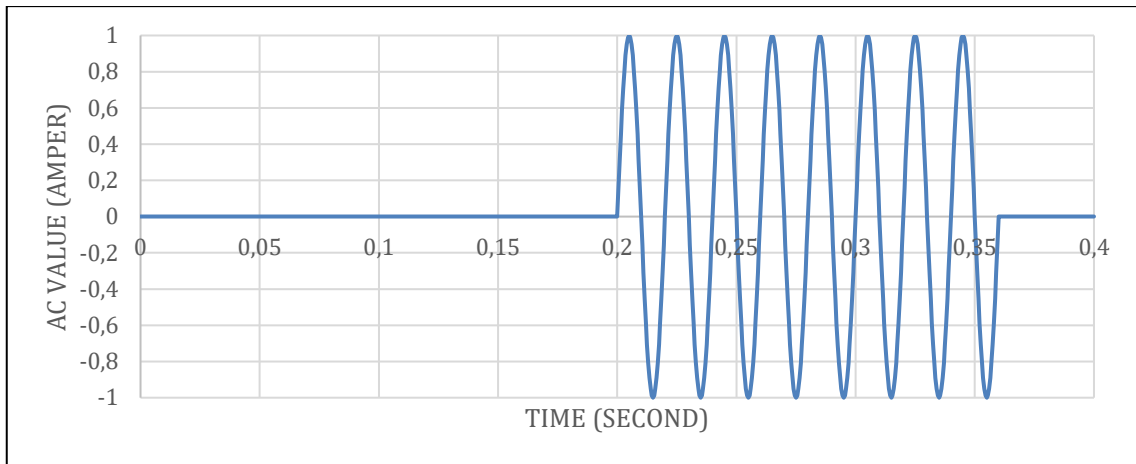
Figure 4. 12.Ideal Sinusoidal Current Value With Respect To Time

Welding equipment consisted of welding machine and computer display which is located in Hacettepe University. Photograph of welding machine with water-cooled was depicted in Figure 4.13. The computer display, connected to the welding machine, allows number of cycle of all stages (which are squeezing, welding and, cooling) to be entered. This welding machine can apply from 7000 up to 10000 ampere phase shifted AC and ideal AC was not applied by welding machine to workpiece due to capacitor effects in high level magnitude of applied current. In experimental parts of this study, 8 kA phase shifted current values were applied to join of MS1500 workpieces during 8 welding cycle.

Figure 4. 13. Photograph of Welding equipment

During experiments, a pedestal AC type welding machine with capacity of 50 kVA, equipped with numerical unit was used. A phase difference caused by the welding machine was observed during welding time. The phase difference values which are obtained from the welding machine measurement were depicted below in Table 4.16. This real sinusoidal electrical current value is called phase shifted alternative current, and in Figure 4.14 was shown. 7; 7.5; 8; 8.5; 9; 9.5, 10 kA phase shifted current values belonging to the different simulation model values, were used to be simulation parameters. Table 4.17 depicts parameters of the simulation model for the RSW process.

Table 4. 16.   The Phase Shift For All Cycles in pedestal AC type welding machine

Cycle Number	The Phase Shift	The Phase Shift Time
1.CYCLE	48°	2.6667 ms
2.CYCLE	46°	2.5556 ms
3.CYCLE	46°	2.5556 ms
4.CYCLE	45°	2.5 ms
5.CYCLE	42°	2.3333 ms
6.CYCLE	40°	2.2222 ms
7.CYCLE	39°	2.1667 ms
8.CYCLE	38°	2.1111 ms

Table 4. 17.   Parameters of the RSW Simulation Models

PARAMETERS	VALUE
IDEAL CURRENT (kA)	8
PHASE SHIFTED CURRENT (kA)	7; 7.5; 8; 8.5; 9; 9.5; 10
WELDING CYCLE	8 CYCLE
COOLING CYCLE	2 CYCLE
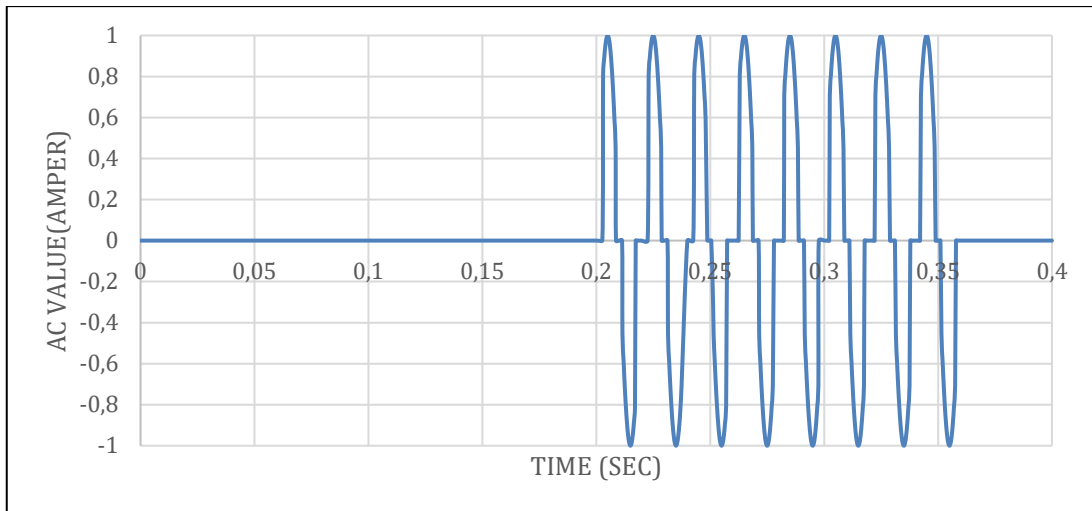
Figure 4. 14.Phase Shifted Current Value With Respect To Time

The FE model of the RSW process consisted of 3 load cases, which are squeezing, welding, and cooling. Moreover, load case property was defined as transient-steady state-static. The existence of more than one load case enables activating boundary conditions for each load case to users. The squeezing load case time was over 0.2 seconds and constant for all simulation models and the time step belonging to the squeezing load case was defined as 50. During the squeezing load case, current/thermal boundary conditions were not activated. The welding load case time was over 0.16 seconds for 8 cycles of applied current (8*0.02 sec=0.16 sec). During the welding load case, joule point current and fixed voltage (lower end of the lower electrode) were activated. The cooling load case took 0.04 seconds (for 2 cooling cycles). During the cooling stage, the coolant temperature and the current were still active, but the applied current value between 0.36 sec and 0.4 sec is zero. Time steps of the welding and cooling load cases were defined to be 100-time steps for each 0.02 second as 800, and 200, respectively. Contact table is activated during all load cases, and resistance calculation is made allowances for sheets during welding stages. The total RSW process time was 0.4 seconds including squeezing, welding, and cooling. The subsequent part of the simulation is the job part in which initial loads, sequence of the load cases, and analysis dimension can be qualified. The heat generation factor was activated and assumed as 0.95 under the job parameters heading. The temperature unit for all simulations was used as Kelvin. For all FE calculations, small strain was assumed. Type 10 element was chosen as an axisymmetric element type.

At the end of the processing part, the exit number shows 3004 on the run job screen, and the meaning of this number is that this simulation ended successfully. The post-processing part shows FEM results, which will declare in the results part of this thesis.

5. RESULTS

The first step of this study was the construction of the FE model of the RSW process. All process of the simulation was declared clearly under the finite element model heading and the basic reference simulation model was set up successfully. The second step was to decide on the type of the current to be applied which are ideal alternative current or alternative current with a phase shift (or phase shifted current). At this stage, the FE results which were constructed with ideal current, and phase shifted current compared with experimental results. This study aims to convergence of the Finite Element (FE) models for the real RSW process by comparing simulation results to physical experiments. In this way, a more realistic option for the alternative current will be illuminated by the experimental results.

5.1. Experimental Result for 8 kA Phase Shifted AC

The experimental results clearly show the nugget shape, nugget dimension, and contact areas between W/W, and W/E at the end of different welding cycles. These results are a guide to whether the nugget shape formed. When MS1500 arrived at the melting temperature which was about 1690 Kelvin, the boundary of the welding nugget was realized obviously.

The experimental images of the selected welding cycles which are located in Figure 5.1.a to Figure 5.1.e, belong to 8 kA phase shifted AC, moreover, these figures give information about welding cycle in which the nugget shape forms. At the end of the 1st and 2nd welding cycles, workpiece/workpiece and workpiece/electrode contact areas were shown in Figure 5.1. a, and Figure 5.1. b, respectively. The experimental results show that nugget formation comes into existence at the end of the 2nd welding cycle. Nugget shape was realized in Figure 5. 1. c, Figure 5.1. d, and Figure 5.1.e. Table 5.1 indicates W/W, W/E contact lengths, and nugget dimensions for selected cycles which belong to the experimental results in tabulated format.

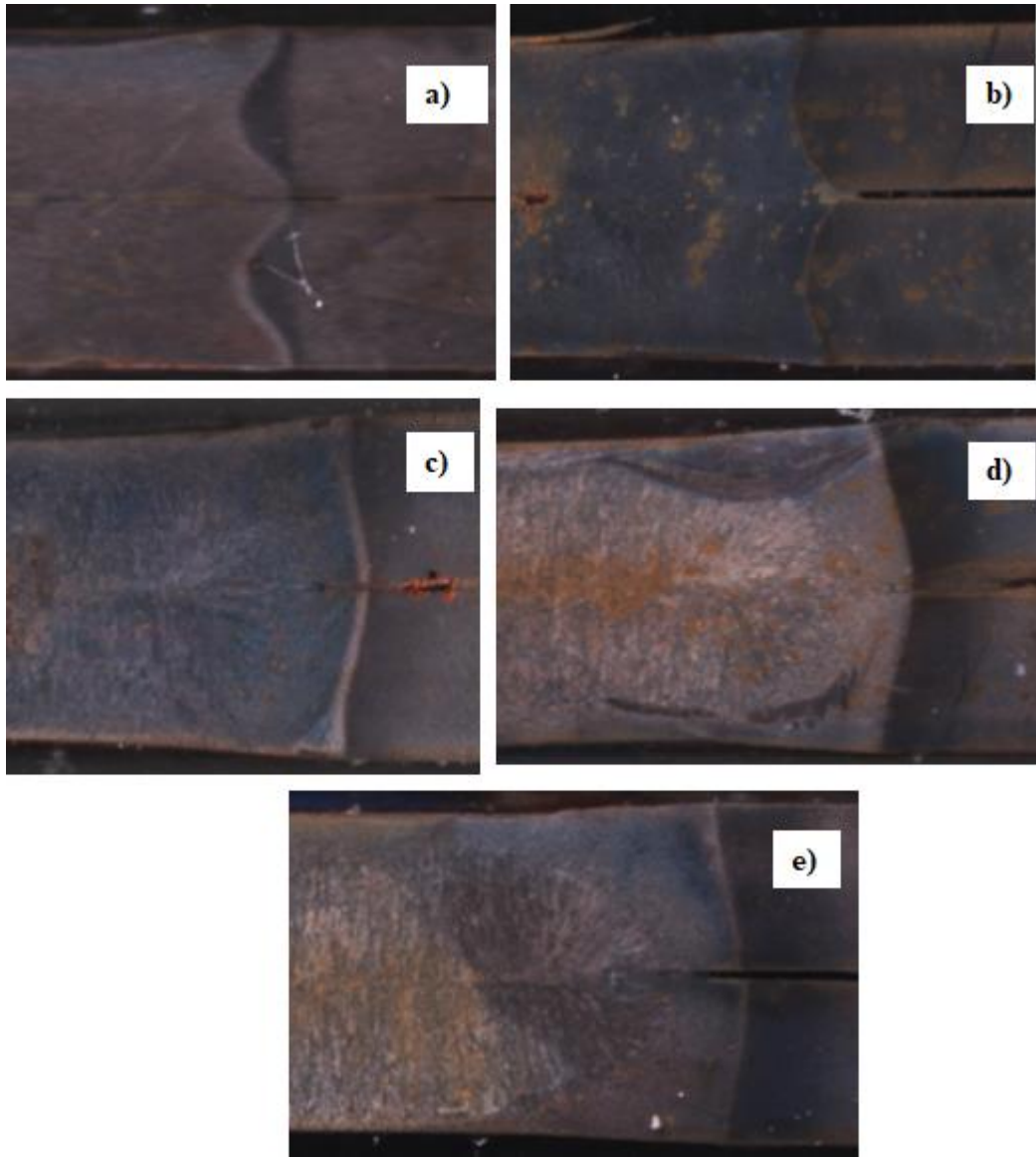Figure 5. 1.Image from the experimental results a) at the end of the 1st welding cycle b) at the end of the 2nd welding cycle c) at the end of the 4th welding cycle d) at the end of 6th welding cycle e) at the end of the 8th welding cycle

Table 5. 1.   W/W and W/E contact length, nugget diameter, and nugget thickness values
in   selected welding cycles of experimental results

Weld. Cyc. Nu. / Time [s]	Nugget Diameter (mm)	Nugget Thickness (mm)	W/W and W/E Total Contact Length (mm)
1.Cyc (0.22 s)	-	-	≈ 4.00
2.Cyc (0.24 s)	-	-	≈ 4.7
4. Cyc (0.28 s)	≈ 3.85	≈ 0.86	-
6. Cyc (0.32 s)	≈ 4.84	≈ 1.5	-
8. Cyc. (0.36 s)	≈ 5.49	≈ 2.00	-

5.2. Finite Element Results for constructed simulation with 8 kA Ideal AC and 8 kA Phase shifted AC

The heat generation amount can be calculated for each welding condition through Joule law. The heat generation amount for the ideal sinusoidal alternative current is higher than the phase shifted current one during welding time because the ideal sinusoidal current was applied in a larger time interval. The applied current value will affect the maximum temperature value for each welding cycle. The heat generation value is directly proportionate to the current value and the square of welding time. So, joule law mathematically states that the ideal alternative current creates more energy input for the welding cycle.

The next step was a comparison of temperature values at the end of the selected cycles which belong to the constructed simulation models with 8 kA ideal AC, and AC with a phase shift (phase shifted current). So far, the data from the experimental results have been limited to the W/W and W/E contact lengths, and nugget dimensions. Extra devices are needed to measure the temperature distribution at the end of the selected welding cycles. Concordantly, the predicted temperature distributions and temperature values at the end of the welding cycles can only be obtained from the simulation results. The predicted temperature values of the selected welding cycles were given for 8 kA ideal AC and 8 kA phase shifted current. These value differences in the selected cycles were seen

in Table 5.2. When these results were compared with experimental results, simulation with constructed ideal AC arrived betimes maximum temperature than expected.

The nugget formation between W/E in the simulation with constructed 8 kA ideal alternative current was observed because the temperature value between workpiece/electrode arrived at 1690 Kelvin. Figure 5.2 shows this unwanted nugget formation between workpiece/electrode in the simulation with constructed 8 kA ideal AC (in 0.337 sec.). Figure 5.3 shows the nugget formation between the workpiece/electrode at the end of the 8th welding cycle. It is seen that the formed nuggets between W/W and W/E merged at the end of this cycle.

Table 5. 2. Comparison of the temperature values which belong to constructed simulation model with ideal 8 kA alternative current and phase shifted current

Weld. Cyc. Nu.	Inc. / Time [s]	Temp. Values for Ideal AC [K]	Temp. Values for Phase Shifted AC [K]	Weld. Cyc. Nu.	Inc. / Time	Temp. Values for Ideal AC [K]	Temp. Values for Phase Shifted AC [K]
1st	150 inc. / 0.22 s	1153	976	5th	550 inc. / 0.30 s	2016	1942
2nd	250 inc. / 0.24 s	1717	1503	6th	650 inc. / 0.32 s	2051	1998
3rd	350 inc. / 0.26 s	1862	1786	7th	750 inc. / 0.34 s	2091	2030
4th	450 inc. / 0.28 s	1952	1874	8th	850 inc. / 0.36 s	2156	2050

Figure 5. 2.Nugget formation between workpiece/electrode and workpiece/workpiece in 0.337 sec of the constructed simulation (8 kA ideal AC)
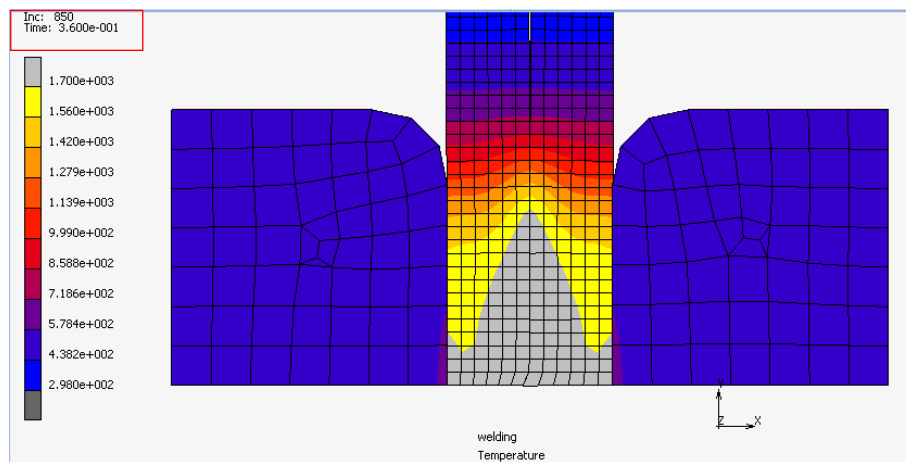
Figure 5. 3.Nugget formation at the end of 8th cycle between workpiece/workpiece constructed simulation with 8 kA Ideal Alternative Current

Figure 5. 4 indicates the nugget formation between the workpiece/workpiece in the simulation with constructed 8 kA phase shifted current. This figure in 0.337 second (same simulation second in Figure 5.2) of the constructed simulation indicates differences contact area where the nugget is formed for phase shifted AC. The unwanted nugget formation between W/E in the simulation was not observed.
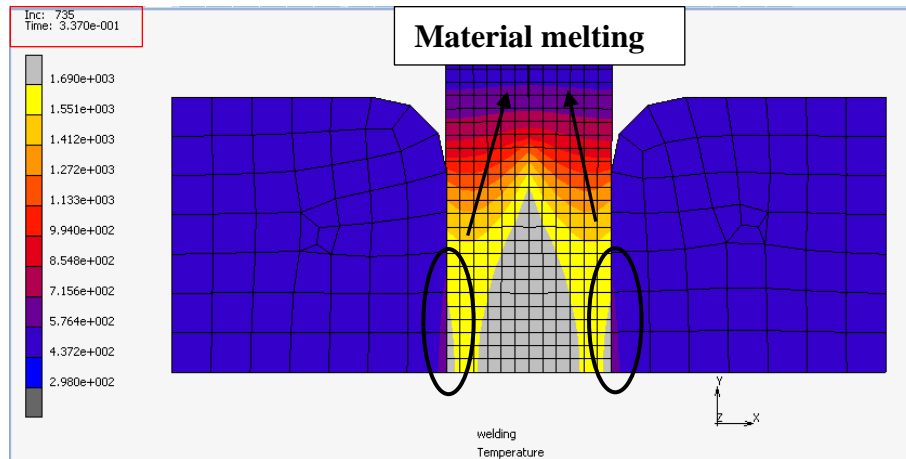
Figure 5. 4. Nugget formation between workpiece/electrode and workpiece/workpiece in 0.337 sec of the constructed simulation (8 kA phase shifted AC)
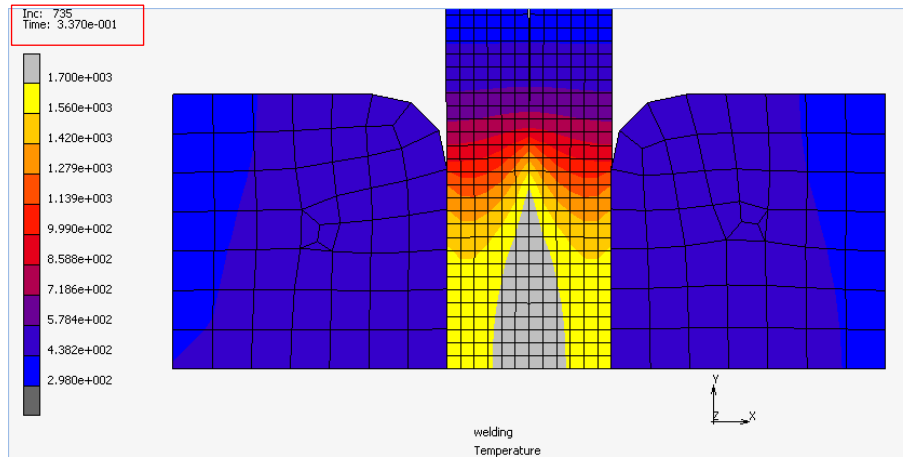
The simulation results show that the heat generation amount for the ideal sinusoidal alternative current is higher than the phase shifted current one during welding time. Comparing the simulation results with physical experiments, the alternative current with phase shift was preferable to constructing the FE model of the real RSW process. After this, all simulation models will be constructed with the phase shifted alternative current.

5.3. Experimental Results and Finite Element Results of constructed simulation with 8 kA Phase shifted AC

In Figure 5.5 to Figure 5.9, experimental, and simulation results were shown side by side in selected welding cycles. Nugget diameter, nugget thickness, W/W, and W/E total contact lengths for selected welding cycles which belong to constructed simulation results with 8 kA phase shifted current depicted below in Table 5.3. Moreover, error calculations are involved in this table. In error calculations, the values obtained from the simulation results constructed with 8 kA phase shifted current were compared with experimental results.

According to the simulation results, at the end of the 1st cycle, the total contact lengths of W/W, and W/E were 6.4 mm, and 5.1 mm, respectively. In the light of the data obtained from Table 5.1, the W/W and W/E total lengths equal to 4 mm. When the experimental and simulation results were compared, the shape of heat temperature distribution

resembled in many aspects nonetheless, when the contact lengths were compared, errors of 27 % and 60 % were available for W/E, and W/W contact lengths, respectively. The predicted temperature distribution information from simulation results and contact areas between sheets at the end of the 1st welding cycle was shown in Figure 5.5.

Figure 5. 5.Comparing the W/E and W/W contact lengths at the end of the 1st welding cycle through experimental and simulation results (8 kA phase shifted current was applied)

Figure 5.6 indicated the comparison of the W/E and W/W contact lengths at the end of the 2nd welding cycle through experimental and simulation results. According to the simulation results, at the end of the 2nd cycle, the total contact lengths of W/W, and W/E were 6.4 mm and 4.98 mm, respectively. The W/W and W/E total lengths were 4.7 mm which was obtained from Table 5.1. When the experimental and simulation results were compared, the shape of the temperature distribution varied in many aspects, furthermore, when the contact lengths were compared, errors of 6 % and 36 % were available for W/E, and W/W contact lengths, respectively.
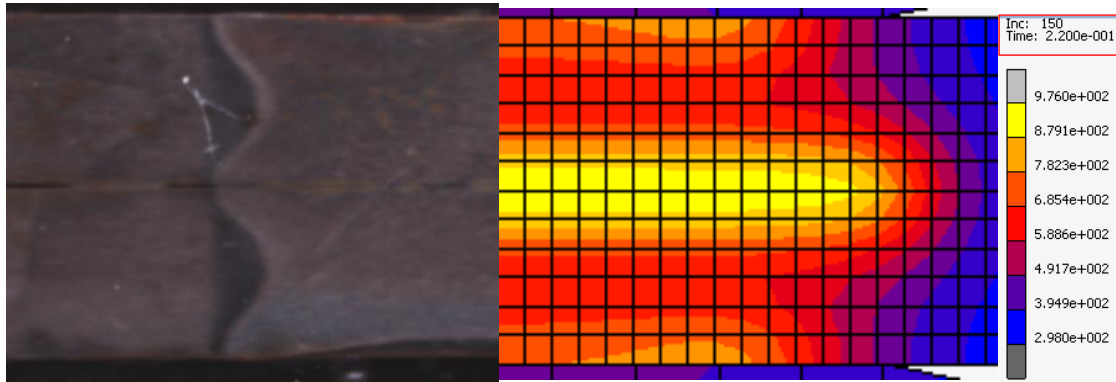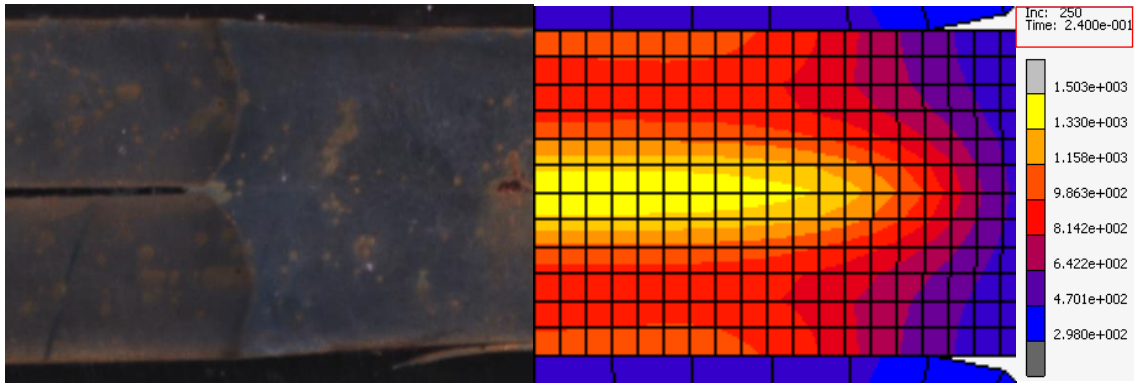
Figure 5. 6.Comparing the W/E and W/W contact lengths at the end of the 2nd welding cycle through experimental and simulation results (8 kA phase shifted current was applied)

After the 4th cycle, nugget shape and nugget dimensions gained importance as comparator parameters rather than W/E and W/W contact lengths, because the temperature formed between workpieces in this cycle melting has already been reached the melting temperature of MS1500. The formed nugget in Figure 5.7 was shown as light grey. At the end of the 4th cycle, the nugget diameter is 4.22 mm whose error is 9 % when compared to the experimental results. Figure 5. 7 indicates the comparing the nugget dimensions at the end of 4th welding cycle through experimental and simulation results.

Figure 5. 7.Comparing nugget dimensions at the end of the 4th welding cycle through experimental and simulation results (8 kA AC with phase shift was applied)

It was observed that the diameter and thickness of the nugget increased in the 6th cycle, and the nugget boundaries can be separated visually in the experimental result. When diameters of nuggets are compared in Figure 5. 8, simulation and experimental results

give close results with an error margin of 4.96 %, but there is an error of 46.6 % when nugget thicknesses are compared. The nugget shape in the below right figure seems like a flat ellipse.

Figure 5. 8.Comparing nugget dimensions at the end of the 6th welding cycle through experimental and simulation results (8 kA phase shifted current was applied)

When comparing the experimental and simulation results in the 8th cycle before the cooling cycles, there is a relatively minor 2% error in the diameter length. The nugget shape in the experimental result was an ellipse, however, the nugget shape in the simulation result was a flat ellipse. Unlike other welding cycles, the length of the nugget diameter was measured in 0.355 seconds of the simulation in the 8th cycle, that is, it is the last peek point of the applied alternative current in the last welding cycle. Figure 5. 9 indicates the comparing the nugget dimensions at the end of 8th welding cycle through experimental and simulation results.

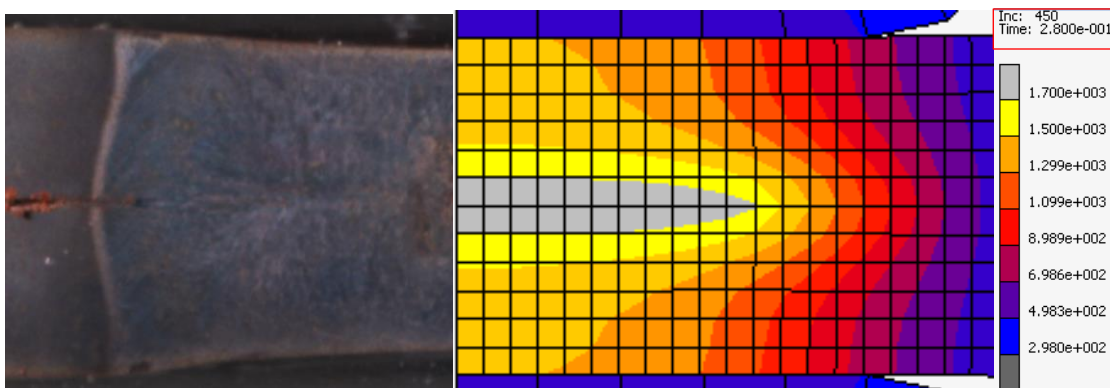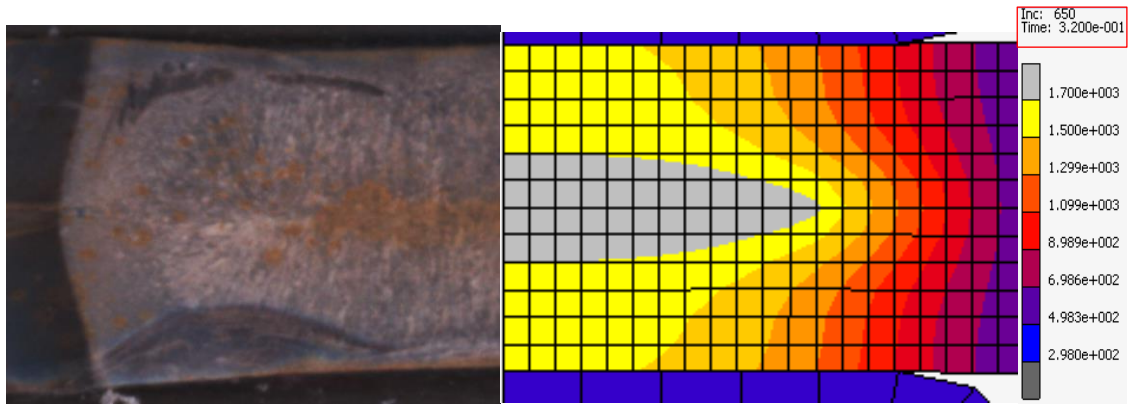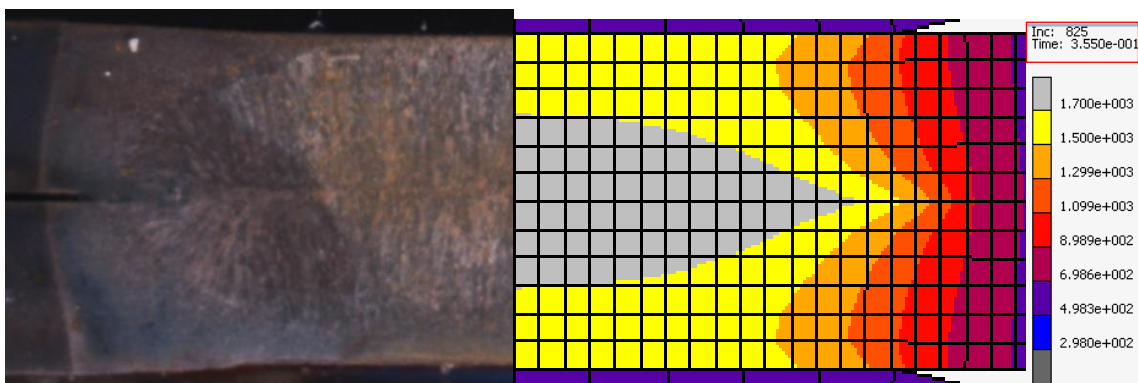Figure 5. 9.Comparing nugget dimensions in 0.355 sec of the 8th welding cycle through experimental and simulation results (8 kA AC with phase shift was applied)

Table 5. 3. Nugget dimension, contact lengths, and error values for selected cycles of the constructed simulation with 8 kA phase shifted AC

Welding Cycle Number/ Time [s]	Nugget diameter (mm)	Nugget thickness (mm)	W/W Total contact length (mm)	W/E Total contact length (mm)	Error (%)
1.Cycle (0.22sec)	-	-	≈ 6.4	≈ 5.1	%27 (for W/E) %60 (for W/W)
2. Cycle (0.24 sec)	-	-	≈ 6.4	≈ 4.98	%6 (for W/E) %36 (for W/W)
4. Cycle (0.28 sec)	≈ 4.22	-	-	-	% 9 (diameter)
6. Cycle (0.32 sec)	≈ 4.6	≈ 0.80	-	-	% 4.96 (diameter) %46.6 (thickness)
8.Cycle (0.355 sec)	≈ 5.38	≈ 1.20	-	-	%2 (diameter) %40 (thickness)

5.4. Finite Element Results for Constructed Simulation with 7; 7.5; 8.5; 9; 9.5; 10 kA Phase Shifted AC

Phase shifted current values 7; 7.5; 8.5; 9; 9.5 and 10 kA for different simulation models were used as simulation parameters and all phase shifted current values were applied to the upper electrodes during 8 welding cycles in the constructed simulations. In this study, simulations created with these simulation parameters have been examined in accordance with FE methods. Simulation results provided information about temperature distributions, nugget sizes, contact length between W/W and W/E, and nugget formation between W/E in the desired simulation second. First, the results of the simulation constructed with a phase shifted current of 7 kA have been analyzed.

Figure 5. 10.Image from the constructed simulation with 7 kA phase shifted current a) at the end of the 1st welding cycle b) at the end of the 8th welding cycle

In Figure 5. 10.a, the predicted temperature distribution at the end of the 1st welding cycle for 7 kA phase shifted current was shown and the W/W and W/E contact length of the 1st welding cycle was not equal to each other. The diameter of the formed nugget at the end of the 8th cycle was around 4.4 mm and the nugget shape in figure 5. 10. b seems like a flat ellipse. Table 5.4 indicates W/W, and W/E total contact lengths, and nugget dimensions for selected welding cycles.

Table 5. 4. Nugget sizes and contact lengths for the selected welding cycles of the constructed simulation with 7 kA phase shifted AC

Welding cycle number/ Time [s]	Nugget diameter (mm)	Nugget thickness (mm)	W/W total contact length (mm)	W/E Total contact length (mm)
1. Cyc. (0.22 s)	-	-	≈ 6.6	≈ 5.3
2. Cyc (0.24 s)	-	-	≈ 6.2	≈ 4.96
4. Cyc (0.28 s)	≈ 3.06	≈ 0.205	-	-
6. Cyc (0.32 s)	≈ 4.10	≈ 0.60	-	-
8. Cyc (0.355 s)	≈ 4.64	≈ 0.97	-	-

47

According to the constructed simulation results with 7.5 kA, at the end of the 1st cycle, the total contact lengths of W/W, and W/E were 6.48 mm, and 5.34 mm, respectively. At the end of the 1st cycle, the temperature between W/W reached 920 Kelvin, which was depicted in Figure 5.11.a. The formed nugget at the end of the 8th cycle has 4.82 mm diameter with a flat ellipse shape which was shown in Figure 5.11.b. Table 5.5 contains specified nugget dimensions and contact lengths for selected cycles of the constructed simulation with 7.5 kA phase shifted AC.
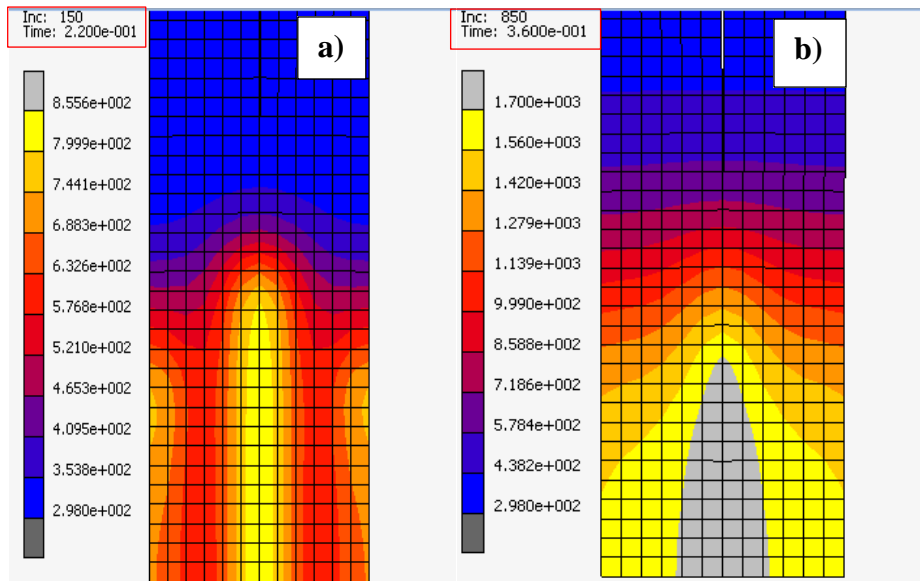

Figure 5. 11.Image from the constructed simulation with 7.5 kA phase shifted current a) at the end of the 1st welding cycle b) at the end of the 8th welding cycle

Table 5. 5.   Nugget sizes, and contact lengths for selected welding cycles of the constructed simulation with 7.5 kA phase shifted AC

Cycle Number/ Time [s]	Nugget Diameter (mm)	Nugget Thickness (mm)	W/W Total Contact Length (mm)	W/E Total Contact Length (mm)
1.Cyc. (0.22 s)	-	-	≈ 6.48	≈ 5.34
2. Cyc. (0.24 s)	-	-	≈ 6.2	≈ 4.68
4. Cyc (0.28 s)	≈ 3.84	≈ 0.33	-	-
6. Cyc (0.32 s)	≈ 4.44	≈ 0.731	-	-
8. Cyc (0.355 s)	≈ 5.1	≈ 1.11	-	-

Predicted temperature distributions at the end of the 1st and 8th welding cycles of the constructed simulation with 8.5 kA phase shifted AC was shown in Figure 5. 12. a and Figure 5. 12. b, respectively. The formed nugget at the end of the 8th cycle has a diameter of 5.38 mm and a flat ellipse shape. The nugget dimensions and contact lengths of the selected weld cycles were listed in Table 5.6.
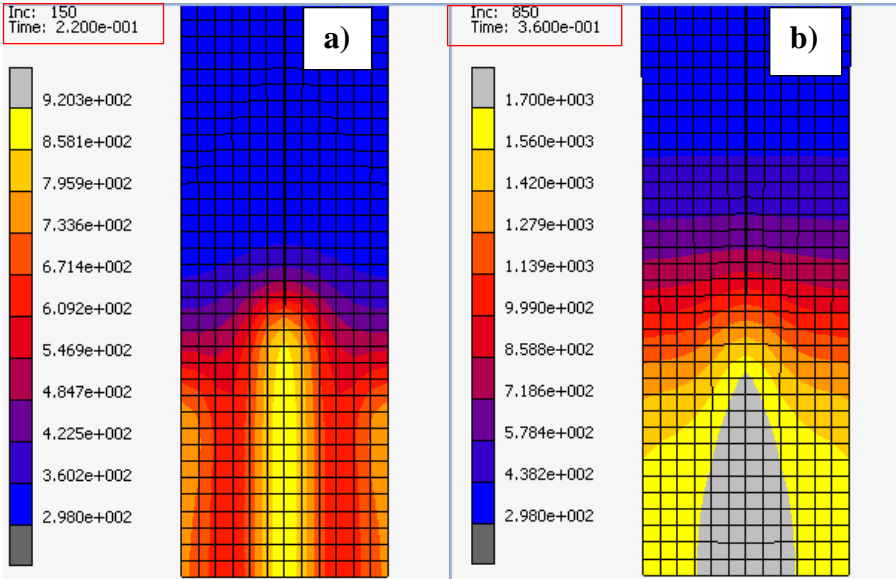

Figure 5. 12.Image from the constructed simulation with 8.5 kA phase shifted current a) at the end of the 1st welding cycle b) at the end of the 8th welding cycle

Table 5. 6. Nugget sizes, and contact lengths for selected welding cycles of the constructed simulation with 8.5 kA phase shifted AC

Welding Cycle Number/ Time [s]	Nugget Diameter (mm)	Nugget Thickness (mm)	W/W Total Contact Length (mm)	W/E Total Contact Length (mm)
1.Cyc. (0.22 s)	-	-	≈ 6.6	≈ 5.82
2.Cyc. (0.24 s)	-	-	≈ 6.5	≈ 5.4
4. Cyc (0.28 s)	≈ 4.6	≈ 0.224	-	-
6. Cyc. (0.32 s)	≈ 5.0	≈ 0.616	-	-
8. Cyc. (0.355 s)	≈ 5.45	≈ 1.07	-	-

In Figure 5. 13. a, temperature distribution at the end of the 1st welding cycle for 9 kA phase shifted current was shown. W/W and W/E contact length for the 1st welding cycle was not equal to each other. The diameter of the formed nugget at the end of the 8th cycle was around 5.44 mm and the nugget shape in Figure 5. 13. b seems like a flat ellipse. Table 5.7 indicates W/W, and W/E total contact lengths, and nugget dimensions for selected welding cycles.
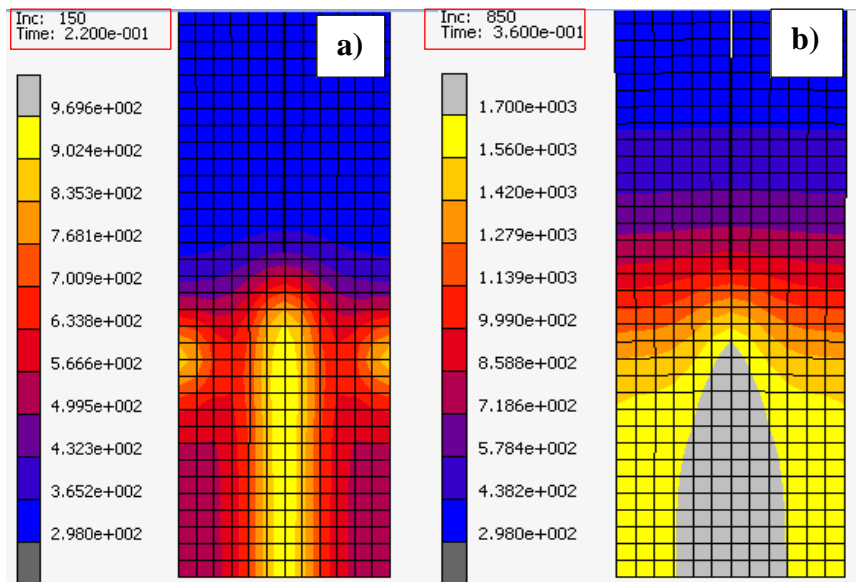

Figure 5. 13.Image from the constructed simulation with 9 kA phase shifted current a) at the end of the 1st welding cycle b) at the end of the 8th welding cycle

Table 5. 7. Nugget sizes, and contact lengths for the selected welding cycles of the constructed simulation with 9 kA phase shifted AC

Welding Cycle Number/ Time [s]	Nugget Diameter (mm)	Nugget Thickness (mm)	W/W Total Contact Length (mm)	W/E Total Contact Length (mm)
1. Cyc. (0.22 s)	-	-	≈ 6.8	≈ 5.82
2. Cyc (0.24 s)	-	-	≈ 6.3	≈ 5.34
4. Cyc. (0.28 s)	≈ 4.98	≈ 0.304	-	-
6. Cyc. (0.32 s)	≈ 5.38	≈ 0.713	-	-
8. Cyc (0.355 s)	≈ 5.76	≈ 1.20	-	-

In Figure 5. 14. a, temperature distribution at the end of the 1st welding cycle for 9.5 kA phase shifted current was shown. The diameter of the formed nugget at the end of the 8th cycle was around 5.57 mm and the nugget shape in Figure 5. 14. b seems like a flat ellipse. Table 5. 8 indicates W/W, and W/E total contact lengths, and nugget dimensions for selected welding cycles.
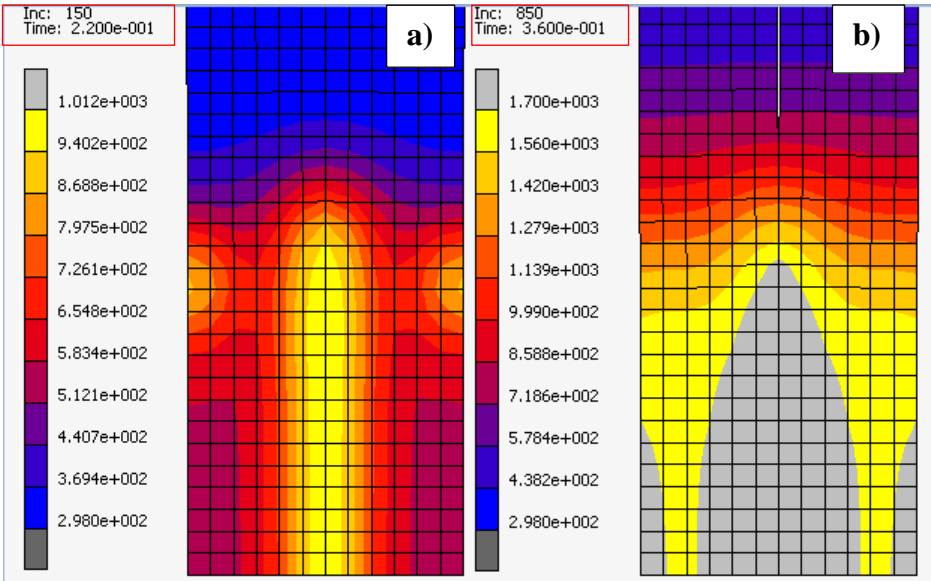

Figure 5. 14.Image from the constructed simulation with 9.5 kA phase shifted current a) at the end of the 1st welding cycle b) at the end of the 8th welding cycle

Table 5. 8. Nugget sizes, and contact lengths for selected welding cycles of the constructed simulation with 9.5 kA phase shifted AC

Welding Cycle Number/ Time [s]	Nugget Diameter (mm)	Nugget Thickness (mm)	W/W Total Contact Length (mm)	W/E Total Contact Length (mm)
1.Cyc. (0.22 s)	-	-	≈ 6.66	≈ 6.1
2. Cyc. (0.24 s)	-	-	≈ 6.5	≈ 5.82
4. Cyc. (0.28 s)	≈ 5.17	≈ 0.37	-	-
6. Cyc. (0.32 s)	≈ 5.45	≈ 0.8	-	-
8. Cyc. (0.355 s)	≈ 5.8	≈ 2.40	-	-

According to the constructed simulation results with 10 kA, at the end of the 1st cycle, the total contact lengths of W/W, and W/E were 6.66 mm, and 6.1 mm, respectively. At the end of the 1st cycle, the temperature between W/W and W/E reached up to 1089 Kelvin, which was depicted in Figure 5. 15. a. The unwanted nugget formation between workpiece/electrode in Figure 5. 15. b was shown due to increasing temperature values between W/E. The formed nugget at the end of the 8th cycle has 5.64 mm diameter.
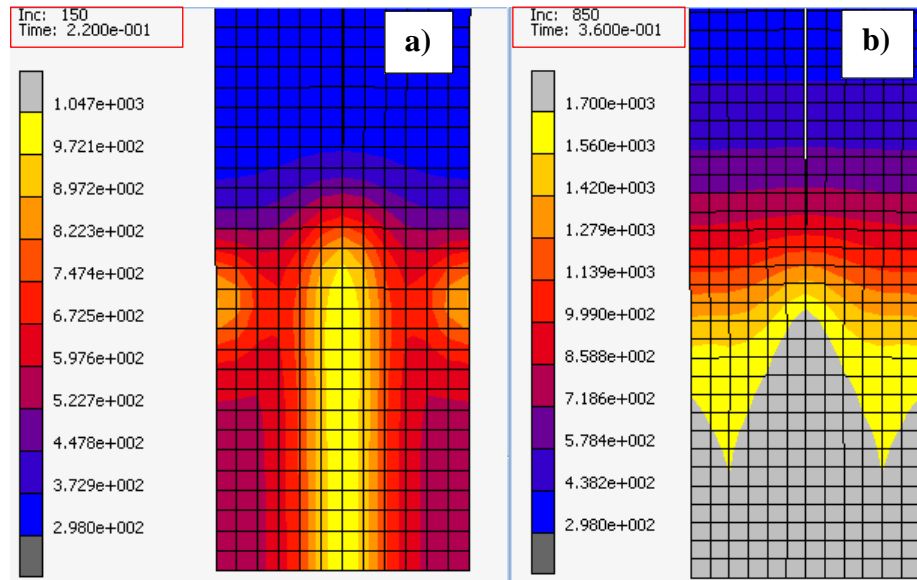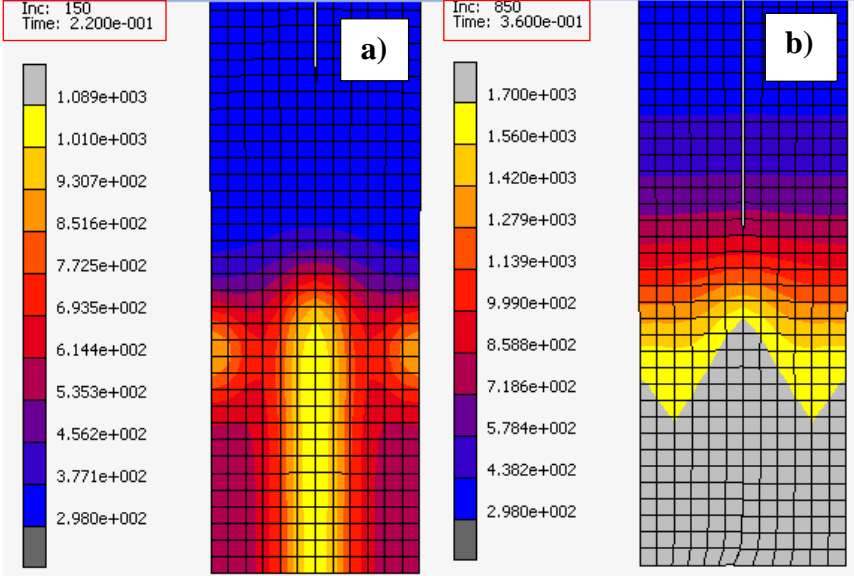

Figure 5. 15.Image from the constructed simulation with 10 kA phase shifted current a) at the end of the 1st welding cycle b) at the end of the 8th welding cycle

Table 5.9 contains the specified nugget dimensions and contact lengths for selected welding cycles of the constructed simulation with 10 kA phase shifted AC. The formed nugget between W/W, and W/E merged at the end of the 8th cycle, which was shown in Figure 5. 15. b. Additionally, the meshes became misshaped after welding cycles.

Table 5. 9. Nugget sizes, contact lengths, and error values for selected welding cycles of the constructed simulation with 10 kA phase shifted AC

Welding Cycle Number/ Time [s]	Nugget Diameter (mm)	Nugget Thickness (mm)	W/W Total Contact Length (mm)	W/E Total Contact Length (mm)
1.Cyc. (0.22 s)	-	-	≈ 6.66	≈ 6.1
2. Cyc. (0.24 s)	-	-	≈ 6.5	≈ 5.82
4. Cyc. (0.28 s)	≈ 5.36	≈ 0.4	-	-
6. Cyc. (0.32 s)	≈ 5.57	≈ 0.940	-	-
8. Cyc. (0.355 s)	≈ 5.88	≈ 2.40	-	-

The entries from Table 5.10 show the temperature values at the selected welding second for 7; 7.5; 8.5; 9; 9.5 and 10 kA simulation parameters. When the temperature values between W/W are examined at the end of all welding cycles, there is a decrease in the rate of temperature rise between 1700 Kelvin and 2000 Kelvin. Due to the decrease in the rate of temperature rise, the specific heat capacity value of MS1500 increases considerably in this temperature range.

Based on the simulation results in Table 5. 11, the nugget diameter increases as the phase shifted AC value increases. However, as the current increases, temperature values between W/W and W/E have increased because the energy input in the welding cycles increases with the square of the current value. As shown in Table 5.11, material melting between W/E was visible in the generated simulation with 8.5; 9; 9.5 and 10 kA phase shifted alternative current.

.

Table 5. 10. Comparison of the temperature values which belong to the constructed simulation model with 7; 7.5; 8.5; 9; 9.5; 10 kA phase shifted alternative current

Cyc. Nu.	Inc.	Temp. values for 7 kA [K]	Temp. values for 7.5 kA [K]	Temp. values for 8.5 kA [K]	Temp. values for 9 kA [K]	Temp. values for 9.5 kA [K]	Temp. values for 10 kA [K]
1st	150	855.6	920.3	969.9	1012	1047	1089
2nd	250	1279	1403	1401	1503	1631	1749
3rd	350	1569	1732	1722	1777	1817	1858
4th	450	1778	1837	1808	1850	1893	1939
5th	550	1842	1901	1876	1922	1965	2008
6th	650	1897	1956	1938	1985	2021	2040
7th	750	1942	2000	1992	2026	2044	2069
8th	850	1980	2027	2026	2047	2081	2143

Table 5. 11. Comparison of the nugget sizes which belong to the constructed simulation models with 7; 7.5; 8; 8.5; 9; 9.5; 10 kA phase shifted current

Simulation Parameter (Phase Shifted AC value) (kA)	Nugget Diameter (850 inc-0.36 s) (mm)	Nugget Thickness (mm)	Melting of Material Between W/E
7 kA	≈ 4.4	≈ 0.913	NO
7.5 kA	≈ 4.82	≈ 1.19	NO
8 kA	≈ 5.00	≈ 1.2	NO
8.5 kA	≈ 5.38	≈ 1.17	YES
9 kA	≈ 5.44	≈ 1.373	YES
9.5 kA	≈ 5.57	≈ 2.4	YES
10 kA	≈ 5.64	≈ 2.4	YES

6. DISCUSSION

At the beginning of the FE model construction, the alternating current type to be applied as a parameter was determined through the FE simulation results (8 kA ideal sinusoidal AC or 8 kA phase shifted AC). Two main simulations were created, by changing the type of applied AC, and the nugget formed in different contact areas. The generated simulation with the ideal sinusoidal current has nugget formation between W/E contact area since temperature values between W/E reached up to melting point of MS1500 sheets. During the welding cycles, ideal sinusoidal current has been applied for longer time and the heat generation has been produced to be proportional to the square of the current value. On the other hand, no nugget formation was observed between W/E in the generated simulation with phase shifted AC. With all these comparisons, the alternative current with phase shift was preferable to constructing the FE model of the RSW process. Starting from this point of view, alternative current type was a crucial parameter to construct the FE modeling of the RSW process.

When comparing the experimental results and the results of generated simulation with 8 kA phase shifted current, there is a relatively minor 2% error in the diameter length and 40% error in nugget thickness at the end of the welding cycles. According to these results, the generated simulation was successful in estimating the nugget diameter, but the nugget thickness has the significant margin of error in this study. The nugget shape in the experimental result was an ellipse, however, the nugget shape in the simulation result was a flat ellipse. That deviation may be result of the inaccuracies in the modelling of thermal properties of the material depending on temperature. During RSW, temperatures exceeding the melting point is observed in metals to be joined. Determination of the properties in these temperature regions require further investigations at very high temperatures. Moreover, phase transformations during heating were not taken into consideration during material formation in these simulations.

As previously mentioned in the FE section, the rigid-meshed body refers to the upper copper electrode in this context, there is a lack of body control of the rigid-mesh body. Load control is not supported by the MSC. Marc interface. This situation has caused the

applied force to change in each increment due to the thermal expansion in the workpiece, with the temperature in the welding cycles. Setting the force value of each current value at each increment would allow the simulation results to achieve values closer to experimental results.

During the RSW process, it is difficult to measure the electrical contact resistances and bulk resistance of materials due to the magnetic field caused by the alternative current. Similarly, experimental equipment is needed to learn about the temperature distribution at the end of the welding cycles. This study provides information on temperature distributions and nugget dimensions thanks to the constructed simulations.

7. SUMMARY AND OUTLOOK

This study includes an examination of the resistance spot welding process of the ultra-high-strength steel (MS1500) with experimental and numerical methods. MSC Marc software has made it possible to construct the FE model for thermo-electro-mechanically coupled FE model, but the fact of not controlling the upper electrode by force, limited constructed simulations on this point. The rigid meshed model for the copper electrode modeling strategy was preferred and workpieces were modeled as meshed (deformable) bodies.

The FE model of the RSW process consisted of 3 load cases, which are squeezing, welding, and cooling. Boundary conditions were activated for different load cases. Firstly, the FE model construction, the alternating current type to be applied as a parameter was determined through the FE simulation results and two main simulation were generated with 8 kA ideal sinusoidal alternative current, and alternative current with phase shift to convergence of the FE models for the real RSW process. The alternative current with phase shift was preferable to constructing the FE model of the RSW process.

Secondly, phase shifted current values 7; 7.5; 8.5; 9; 9.5 and 10 kA for different simulation models were used as simulation parameters. Simulation results provided information about temperature distributions, nugget sizes, contact lengths between W/W and W/E, and nugget formation between W/E. Consequently, the nugget diameter increases as the phase shifted current value increases. However, as the current increases, nugget formation between W/E was observed due to temperature values on the rise. As a consequence, material melting between W/E was visible in the generated simulation with 8.5; 9; 9.5 and 10 kA phase shifted current.

Studies showed that nugget diameter can be modeled using electro-thermo-mechanical coupled FE simulations. Nevertheless, due to inaccurate data in the thermal properties of materials at elevated temperatures, nugget thickness couldn't be modeled accurate enough.

In further studies, it is planned to investigate material properties depending on temperature more accurately and improve the accuracy of the simulations.

8. REFERENCES

[1] S. Keeler, M. Kimchi, P. J. Mooney, Advanced High-Strength Steels Apllication Guidelines Version 6.0, World Auto Steel. 6 **(2017)** 314.

[2] N. den Uijl, Resistance Spot Welding of Advanced High Strength Steels, **2013**. https://doi.org/10.13140/RG.2.1.3050.8245

[3] B. V. Feujofack Kemda, N. Barka, M. Jahazi, D. Osmani, Optimization of resistance spot welding process applied to A36 mild steel and hot dipped galvanized steel based on hardness and nugget geometry, Int. J. Adv. Manuf. Technol. 106 **(2020)** 2477–2491. https://doi.org/10.1007/s00170-019-04707-w.

[4] H.A. Nied, The Finite Element Modeling of the Resistance Spot Welding Process An analytical tool is provided to predict the processing parameters needed to produce a spot weld with sufficient joint penetration, Weld. Res. Suppl. **(1984)** 123–132.

[5] H. Huh, W.J. Kang, Electrothermal analysis of electric resistance spot welding processes by a 3-D finite element method, J. Mater. Process. Technol. 63 **(1997)** 672–677. https://doi.org/10.1016/S0924-0136(96)02705-7.

[6] X. Deng, W. Chen, G. Shi, Three-dimensional finite element analysis of the mechanical behavior of spot welds, Finite Elem. Anal. Des. 35 **(2000)** 17–39. https://doi.org/10.1016/S0168-874X(99)00053-0.

[7] B.H. Chang, Y. Zhou, Numerical study on the effect of electrode force in small-scale resistance spot welding, J. Mater. Process. Technol. 139 **(2003)** 635–641. https://doi.org/10.1016/S0924-0316(03)00613-7

[8] W. Zhang, Design and implementation of software for resistance welding process simulations, SAE Tech. Pap. **(2003)**. https://doi.org/10.4271/2003-01-0978.

[9] H. Zhigang, W. Yuanxun, L. Chunzhi, C. Chuanyao, A multi-coupled finite element analysis of resistance spot welding process, Acta Mech. Solida Sin. 19 **(2006)** 86–94. https://doi.org/10.1007/s10338-006-0610-z.

[10] Z. Hou, I.S. Kim, Y. Wang, C. Li, C. Chen, Finite element analysis for the mechanical features of resistance spot welding process, J. Mater. Process. Technol. 185 **(2007)** 160–165. https://doi.org/10.1016/j.jmatprotec.2006.03.143.

[11] H. Eisazadeh, M. Hamedi, A. Halvaee, New parametric study of nugget size in resistance spot welding process using finite element method, Mater. Des. 31 **(2010)** 149–157. https://doi.org/10.1016/j.matdes.2009.06.042.

[12] N.V.. Thakur.AG, Rasane A.R, Finite element analysis of resistance spot welding to study nugget formation, Int. J. Appl. Eng. Res. 1 **(2010)** 5799–5802.

[13] R. Hashemi, H. Pashazadeh, M. Hamedi, An incrementally coupled thermo-electro-mechanical model for resistance spot welding, Mater. Manuf. Process. 27 **(2012)** 1442–1449. https://doi.org/10.1080/10426914.2012.718470.

[14] M. Vural, Finite element analysis of the thermo-mechanical behavior of the resistance spot welding, Usak Univ. J. Mater. Sci. 2 **(2013)** 31–31. https://doi.org/10.12748/uujms/20131710.

[15] M. Design, A. Corporation, T. Kobayashi, Y. Mihara, Numerical Simulation of Nugget Formation in Spot Welding, **(2014)** 1–15.

[16] M. Jafari, A. Arayee, J. Senkara, A Review of Finite Element Analysis (FEA) of Resistance Spot Welding (RSW), Przegląd Spaw. - Weld. Technol. Rev. 88 **(2016)** 46–52. https://doi.org/10.26628/ps.v88i2.571.

[17] T. Kik, M. Slováček, Numerical Analyses in the Modelling of Spot Resistance Welding Processes, Biul. Inst. Spaw. 2017 **(2017)** 17–25. https://doi.org/10.17729/ebis.2017.5/2.

[18] Y. Lee, H. Jeong, K. Park, Y. Kim, J. Cho, Development of numerical analysis model for resistance spot welding of automotive steel, J. Mech. Sci. Technol. 31 (2017) 3455–3464. https://doi.org/10.1007/s12206-017-0634-y.

[19] P. Kah, M. Pirinen, R. Suoranta, J. Martikainen, Welding of ultra high strength steels, Adv. Mater. Res. 849 **(2014)** 357–365. https://doi.org/10.4028/www.scientific.net/AMR.849.357.

[20] C.M. Tamarelli, AHSS 101: the evolving use of advanced high-strength steel for automotive applications, Steel Mark. Dev. Inst. **(2011)** 42.

[21] SMDI: More than 65 Advanced High-Strength Steel Vehicles Debuted in 2018.” *Repairer Driven News*, 8 Jan. 2019, www.repairerdrivennews.com/2019/01/08/smdi-more-than-65-advanced-high-strength-steel-vehicles-debuted-in-2018/ (Date Accessed: **17 April 2022**)

[22] W. Zheng, M. Wang, L. Kong, X. Cheng, M. Lei, Parameter optimization of dissimilar resistance spot welding on ultra-high strength hot-stamped steel and mild steel by numerical simulation, Acta Metall. Sin. (English Lett. 25 **(2012)** 487–498. https://doi.org/10.11890/1006-7191-126-487.

[23] O. Andersson, A. Melander, Prediction and Verification of Resistance Spot Welding Results of Ultra-High Strength Steels through FE Simulations, Model. Numer. Simul. Mater. Sci. 05 **(2015)** 26–37. https://doi.org/10.4236/mnsms.2015.51003.

[24] Z.S. Yu, W.P. Dong, C.W. Ma, J.W. Ren, B.H. Li, Y.R. Ji, Resistance Spot Weldability of Hot-Formed Ultra High Strength Steel Based on Virtual and Physical Experiment, Appl. Mech. Mater. 750 **(2015)** 244–250. https://doi.org/10.4028/www.scientific.net/amm.750.244.

[25] M. Demir, B., İncekar, E., Dincel, Ö., Elitaş, İleri Dayanımlı Çeliklerde Nokta Direnç Kaynağı Etkilerinin İncelenmesi, 2017 **(2017)** 92–100.

[26] X. Wan, Y. Wang, P. Zhang, Numerical simulation on deformation and stress variation in resistance spot welding of dual-phase steel, Int. J. Adv. Manuf. Technol. 92 **(2017)** 2619–2629. https://doi.org/10.1007/s00170-017-0191-7.

[27] "Docol 1500m Martensitli Otomotiv Çeliği." Docol 1500M Martensitli Otomotiv Çeliği, https://www.ssab.com/tr-tr/products/brands/docol/products/docol-1500m. (Date Accessed: **17 April 2022**)

[28] H. Wang, Y. Zhang, Modelling of heat affected zone softening in laser welding of M1500, ASME 2015 Int. Manuf. Sci. Eng. Conf. MSEC 2015. 1 **(2015)** 1–9. https://doi.org/10.1115/MSEC20159251.

[29] "The Online Materials Information Resource" MatWeb http://www.matweb.com/search/DataSheet.aspx?MatGUID=7b75475aa1bc4161 8788f63c6500d36b&ckck=1. (Date Accessed: **17 April 2022**)